MEASUREMENT AND MODELING OF THE IN-PLANE PERMEABILITY OF ORIENTED STRAND-BASED WOOD COMPOSITES

by

Chao Zhang

B.Sc., Tsinghua University, 2006

A THESIS SUBMITTED IN PARTIAL FULFILMENT OF
THE REQUIREMENTS FOR THE DEGREE OF

MASTER OF SCIENCE

in

The Faculty of Graduate Studies

(Forestry)

THE UNIVERSITY OF BRITISH COLUMBIA
(Vancouver)

April 2009

Abstract

The objective of this research is to investigate the effects of panel density and air flow direction on the in-plane permeability of oriented strand-based wood composites. In-plane permeability is a key factor governing the energy consumption and pressing time during manufacture. The result is expected to provide information which could potentially reduce the pressing time.

The thick, oriented strand boards of five densities were made of aspen (*Populus tremuloides*), and pressed in the laboratory. The production procedure yielded a uniform vertical density profile and good strand orientation. The specimens were sealed in a specially designed specimen holder and connected to a permeability measurement apparatus. The permeability values in parallel, perpendicular, and 45° to the strand orientation were obtained.

The results showed that permeability values decreased rapidly as the density increased. The permeability was highest in the parallel-to-strand direction, and lowest in the perpendicular-to-strand direction. The permeability value in 45° direction was between the values of parallel- and perpendicular-to-strand directions. A polynomial equation was fitted to the results and an R^2 was between 0.938 and 0.993.

To examine the void structure changes during the densification, microscopic techniques were employed. Microscopic slides for each density level were prepared with a typical method widely used for petrography, and then investigated with a fluorescence microscope. The compression of inter-strand and intra-strand voids, including the failure of cell walls, was observed. The compression of cell structures was found and a high variability between regions was observed to occur within one specimen.

A model for the permeability in the direction parallel to strand orientation was developed based on the microscopic and macroscopic geometry measurements. The vessel element was considered as the main path for intra-strand fluid transportation and its size development with compression was determined by the microscopic analysis. Permeability was then calculated by the sum of flows occurring intra-strand voids added with the

effect of inter-strand voids. The model predictions closely matched the experimental data for densities between 450 and 700 kg/m^3.

Table of Contents

List of Tables

List of Figures

Acknowledgements

I would like to express my sincere appreciation to my supervisor Dr. Gregory D. Smith. With patient teaching, explaining, and discussion he guided me to the challenging world of wood composites. He provided remarkable support, advice, understanding, and encouragement during the research, especially when failures and frustration came. Without that I would have been lost.

I am grateful to my committee members, Dr. Frank Lam and Dr. Stavros Avramidis, for their suggestions, assistance, and encouragements throughout my study. Their research backgrounds in wood mechanics and wood physics brought me more comprehensive perspectives of wood composites. And their passion and enthusiasm in research is always an example for me and motivates me to continue.

I also would like to thank Dr. Simon Ellis for offering the microscopic equipments, and to thank Mr. Emmanuel Sackey for his teaching of operating laboratory equipment and smoothing out the difficulty that came in the experiments. I wish to thank Mr. George Lee and Mr. Larry Tong for helping me preparing the samples.

Appreciation is also extended to Dr. Kate Semple, Mr. Graeme Dick, and Ms. Solace Sam-Brew for their help and providing a relaxing and fun office environment.

I am indebted to my wife for her unlimited patience and love, and my parents who love me all the time. I cherish the prayer and true friendship from my Christian brothers and sisters.

The financial support from Forestry Innovation Investment Ltd. is greatly appreciated. And a special thanks to Ainsworth Lumber Canada Ltd. for providing the strands, to Hexion Canada for the PF resin, and to Forintek Canada Corp. (Vancouver) for the use of their facilities.

1 Introduction

Commercial wood composite products are produced from various kinds of wood elements: veneer, strand, particle, and fiber. Plywood and laminated veneer lumber (LVL) are made from veneer sheets; oriented strandboard (OSB) and oriented strand lumber (OSL) are composed of strands; particleboard is made of particles; and medium density fiberboard (MDF) is composed of fibers.

OSB is a kind of strand-based wood composites widely used for structural sheathing purposes in the residential construction. The production of OSB in North America was 21.18 million m^3 in 2007, with a share of 59.4% in structural panel market (UNECE 2009). However, after the OSB price soared to US$668 per m^3 (US$591 per thousand square feet) in April, 2004, it started to drop and hit a record low of US$198 per m^3 (US$175 per thousand square feet) in March, 2007, as shown in Figure 1.1 (Random Lengths 2008).

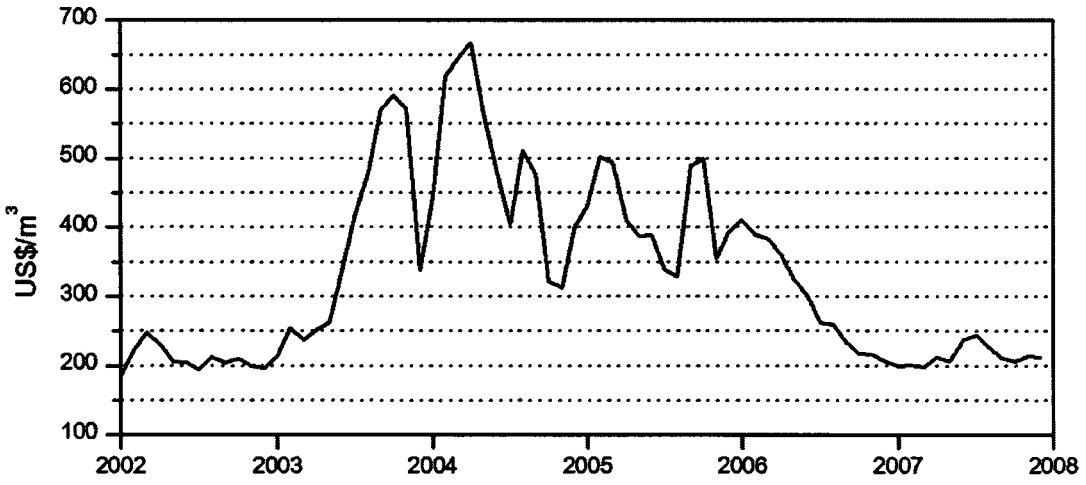

Figure 1.1: OSB price in North America 2002-2007 (Source: Random Lengths 2008).

The decrease was mostly the result of the weak US housing starts. Single-family housing starts in US, which dropped from 2.1 million in 2005 to 1.6 million in 2007, were forecasted to be below 1 million in 2008 for the first time in almost 40 years. During the year 2007, the net loss of OSB production capacity in North America was 870,000 m^3 as

a result of the closure of four mills (three in Canada and one in US). The OSB manufacturers recorded only 88% of their production capacity in use, the lowest level since the early 1990s (UNECE/FAO 2008). The OSB production decreased to 18.010 million m^3 in 2008, and is forecasted to be 17.668 million m^3 in 2009 (UNECE 2009).

The US housing collapse and resulting downturn in credit and financial markets in 2008 brought US to the deepest recession in a generation. Many factors will intensify the uncertainty of OSB market including: a deeper and more severe recession than expected, and a higher number of foreclosures. Very weak market conditions have resulted in negative profit margins across the structural panel industry, and profitability will be more restrained in 2009 and 2010 (RISI 2008).

The panel manufacturers also have to face the increasing cost for nearly all cost factors, including wood, resins, energy, and labor. Based on the report from UNECE/FAO (2007), wood and glue prices increased more than 20% in 2006 as a result of the tight competition with the biomass industry and soaring oil prices. The table below shows the increasing cost of input factors to manufacture OSB from 2000 to 2006: all the cost items increased drastically in the seven years, especially for diesel whose price doubled. The oil prices rose dramatically over the last year and reached $139 per barrel in June 2008, providing a greater incentive for decreasing energy consumption. Although it started to fall in the third quarter 2008, the oil price will increase in a long term as a result of high demand and oil shortage.

Table 1.1: Approximate costs for various OSB manufacturing inputs for a north-central US location, 2000-2006 (adapted from Spelter et al. 2006).

Cost item	Cost (US$/unit)						
	2000	2001	2002	2003	2004	2005	2006
Wood (m^3)	30	28	28	32	36	46	44
Labour (h)	21.7	22.7	23.9	25.1	26.2	27.5	28.3
Liquid PF (kg)	0.79	0.83	0.82	1.15	1.17	1.39	1.26
Wax (kg)	0.82	0.82	0.82	0.87	0.88	1.01	0.97
Nat gas (GJ)	4.1	4.9	3.8	5.3	6.1	7.6	7.4
Electricity (kWh)	0.036	0.043	0.045	0.055	0.058	0.060	0.062
Diesel (L)	0.26	0.25	0.23	0.28	0.35	0.48	0.53

Therefore, as the OSB manufacturing companies are facing more and more pressure from increasing cost, shrinking markets and stronger competition, there is a need to reduce material costs and improve production efficiency.

1.1 Rationale

Hot-pressing is one of the most important processes in the manufacture of strand-based wood composites. Applying high temperature and pressure, a loosely formed resinated strand mat is compressed to a target thickness and density. The heating of strands leads to water vaporization and increased internal gas pressure, which should be transferred out of the mat before the end of the press. The heat and gas flow through a panel is significantly affected by the changes in permeability during consolidation. As the productivity of a press is determined by the amount of time it takes to process each batch of panels, permeability is the key factor to optimizing the press cycle time, throughput, and production cost.

In addition to local density, the permeability of strand-based wood composites is also affected by wood element size and void structure. The effects of core fines content and mat density on transverse permeability of OSB has been investigated by Fakhri *et al* (2006a, b). Hood *et al.* (2005) reported transverse and in-plane permeability of unresinated strand panels.

To date there has been little work that addressed in-plane permeability of thick, oriented and resinated strand based wood composites during the panel consolidation. The work presented here is aimed to fill this gap and has the following objectives.

1.2 Objectives

1. Development of a methodology for measuring the in-plane permeability of thick, strand-based wood composites.
2. Assessment of the effects of air flow direction relative to strand orientation and board density on specific permeability.

3. Investigation of void geometry changes during consolidation by microscopic techniques.
4. Development of a physical model that predicts permeability based on the microscopic and macroscopic geometry measurements.

2 Literature Review

2.1 Hot-pressing process

The purpose of hot-pressing is to consolidate the loose, resinated strand mat into a finished panel of the correct density, thickness, strength, and stiffness in addition to other properties. The contact surface area between wood elements increases during compression to final thickness. As the temperature increases the resin cures and wood elements are bonded together. During this period, complex heat and moisture transfer occurs in the mat.

2.1.1 Heat transfer

The press platens are heated by oil or stream. Heat transfers from the platens to the mat by conduction and convection. Conduction is the transfer of heat energy through a solid from a region of high temperature to low temperature within the body due to vibrations of its atoms or molecules; if heat is to transfer from body to body, it is necessary that these bodies be in direct, intimate contact. Convection is the transfer of heat in a gas or liquid due to density difference in the fluid. In the case of hot-pressing, heat is transferred by a combination of conduction and convection. When the strand mat is compressed between heated platens, heat is transferred by conduction into those strands in contact with the platen. As the strand mat is heated, the absorbed moisture in the strand vaporizes and flows through the voids between adjacent strands and to a much less degree through strands themselves. As these heated gases move, they in turn heat strands by convection.

The conduction through the mat for a steady state and one-dimensional case is expressed as Fourier's first law:

$$q_{th} = -k_{th} \frac{dT}{dx} \qquad (2.1)$$

where q_{th} is the heat flux (J s^{-1} m^{-2}), k_{th} is the mat thermal conductivity (J s^{-1} $°C^{-1}$ m^{-1}), T is the temperature (°C), and x is the distance (m) through which the heat flows.

The assumption of steady state, which means constant temperature distribution over time, is not valid for hot-pressing process. For transient heat flow the relevant equation is

$$\rho c \frac{dT}{dt} = k_{th} \frac{d^2T}{dx^2} \qquad (2.2)$$

where ρ is the mat density (kg m^{-3}) and c is the specific heat of the mat (J kg^{-1} $°C^{-1}$). The left side of the equation has units of energy change per second per unit volume.

Zombori *et al.* (2003) pointed out that the thermal conductivity of the wood composites varies with the mat structure (flake density, flake orientation, void fraction) and with the internal environment. Hood (2005) mentioned for wood composites thermal conductivity was directly proportional to density for densities below 1000 kg m^{-3}. Humphrey and Bolton (1989) presented an equation to estimate the thermal conductivity of particleboard in transverse direction:

$$k_{th} = (0.01172 + 0.0001319\,\rho) F_m F_t \qquad (2.3)$$

where F_m is a correction factor for moisture content where $F_m = 0.00103 M_c + 1.00000$, M_c is the moisture content of board material, F_t is a correction factor of temperature $F_t = 0.001077T + 0.978$, T is temperature in degrees centigrade, and ρ is the oven-dry density (kg m^{-3}).

Bolton and Humphrey (1988) stated that the main mechanism of heat transfer was by convection. Based on the previous work (Bowen 1970, Kavvuras 1977, Denisov and Sosnin 1967, and Strickler 1959), Humphrey and Bolton (1989) described the convection process: the heat transferred into the mat causes the vaporization of furnish moisture and increasing the water vapor pressure. This creates a vapor pressure gradient across the board thickness and in turn causes flow that transfers the heat content of vapor. Meanwhile, an outward or radial pressure gradient is also established, causing in-plane heat transfer and vapor and heat loss from the edges of the board. Therefore, the convection is not only affected by heat, but also by mass transfer in the mat.

2.1.2 Moisture transfer

The moisture transfer during the hot-pressing is mainly concerned with the steam generated by the high temperature flowing out of the mat edges. The gaseous flow is transported by bulk flow due to total pressure differential and diffusion due to partial pressure differential. Darcy's law and Fick's law are used to describe the bulk flow and diffusion component. Based on this assumption, Zombori *et al.* (2003) presented a combination of Darcy's law and Fick's law for the transport mechanism for the vapor phase:

$$n_v = -K_m \frac{\partial}{\partial x}(P) - D_m \frac{\partial}{\partial x}\left(\frac{p_v}{P}\right) \qquad (2.4)$$

where n_v is the vapor flux (kg m^{-2} s^{-1}), K_m is the mat superficial gas permeability (s), D_m is the mat gas diffusivity (kg m^{-1} s^{-1} Pa^{-1}), P is the total pressure (Pa), p_v is the partial pressure (Pa), and x is the distance of the transfer (m). Furthermore, Zombori *et al.* (2003) pointed out that the rate of bulk flow and diffusion of vapor through the mat is determined by the mat superficial permeability K_m and the mat diffusivity D_m, which depend on the specific permeability K_g (m^3/m) and effective diffusivity D_{eff} (m^2/s) respectively. The two factors are functions of void geometry in the mat only and independent of the fluid properties.

2.1.3 Investigation and modeling

Humphrey and Bolton (1989) developed a theoretical model to describe the heat and moisture transfer for particleboard during hot-pressing. The model predicted the temperature, water-vapor pressure, equilibrium moisture content, and relative humidity based on three independent variables: time, vertical position, and horizontal position within the mat. In successive publications, the variation of temperature, vapor pressure, moisture content, and relative humidity were predicted and were found to be in good agreement with the observations (Bolton *et al.* 1989a,b).

In a series of work done by Oudjehane and co-workers (Oudjehane *et al.* 1998a, 1998b, Oudjehane and Lam 1998), a density model was developed by combining the mass

transfer, consolidation strain, the distribution of flakes, and the density. The formation of strand mats was investigated by simulating the placement of rectangular strands at random locations and random orientations within a given area.

Thoemen and co-workers (Thoemen 2000, Thoemen and Humphrey 2003, Thoemen and Humphrey 2006, Thoemen *et al.* 2006) used the model of Humphrey and Bolton (1989) as a starting point and developed a three-dimensional model to simulate the heat and mass transfer and mat densification during hot-pressing of wood-based composites. Material properties of MDF were used as input parameters and the agreement between predicted and measured data was good. Carvalho and Costa (1998) and Carvalho *et al.* (2003) presented similar models for MDF, which predicted the variables relating to heat and mass transfer (temperature, moisture content, gas pressure and relative humidity) as well as variables relating to mechanical behaviors (pressing pressure, strain, modulus of elasticity and density).

Garcia *et al.* (2001) found that for OSB, panel density positively affected thermal conduction, and negatively affected permeability (both lateral and transverse) and transverse thermal convection, while flake alignment positively affected lateral permeability, and negatively affected transverse thermal convection. In the following work, Garcia (2002) and Garcia *et al.* (2003) investigated the horizontal gas pressure and temperature distribution, and found that: higher density created a steeper temperature and pressure gradient; higher aligned panel yielded higher pressure and temperature difference between the parallel and perpendicular to the flake alignment directions; in addition, increasing the mat density reduced the flake-alignment effect.

Garcia (2002) developed a full mathematical model with a system of partial differential equations for gas pressure, temperature, and moisture content versus time. The model predictions followed trends and behaviors of hot-pressing heat and mass transfer theories. The predicted temperatures were found to closely match the experimental measurements.

Garcia (2002) and Garcia *et al.* (2004) also provided a regression model of horizontal temperature and gas pressure distributions. The model fitted the experimental

measurement of internal temperature and pressure distributions, and the theoretical temperature and pressure distributions predicted by the mathematical model above.

Zombori *et al.* (2003) reported a two-dimensional mathematical model including different heat and mass transfer processes. The model was capable of simulating the change of the internal environment based on the moisture content, temperature, pressure gradient, and the extent of resin cure characterized by the cure index. Dai and Yu (2004) presented a physical-mathematical model for heat and moisture transfer in wood composite mats during hot-pressing. It consists of fifteen governing equations to solve fifteen unknown variables including temperature, gas pressure, and moisture content. With the model, the heat and mass transfer variables were linked to material properties, e.g. mat density, thermal conductivity and permeability.

2.2 General concepts of permeability

Permeability is a measure of the ability to transmit fluids. The steady-state transport of fluid through a porous media can be characterized by Darcy's law which is expressed as flux divided by pressure gradient (Siau 1995):

$$k = \frac{V L}{t A \Delta P} \tag{2.5}$$

where, k is the permeability ($m^2 \cdot Pa^{-1} \cdot sec^{-1}$), V is the volume of fluid flowing through specimen (m^3), L is the length of specimen in the flow direction (m), t is the time of flow (sec), A is the cross sectional area perpendicular to flow direction, (m^2), and ΔP is the pressure drop (Pa) that occurs over length L.

The assumptions of Darcy's law were discussed by Muskat (1946), Scheidegger (1974), and Siau (1995) presented the following ones:

1. The flow is viscous and linear. The volumetric flow rate and linear velocity are directly proportional to the applied pressure gradient.
2. The fluid is incompressible and homogeneous.
3. The porous medium is homogeneous.
4. There is no interaction between the fluid and the substrate.
5. Permeability is independent of the length of the specimen in the flow direction.

Although the assumptions are frequently violated when Darcy's law is applied to the flow of gases and aqueous liquid through wood, the basic equation provides a useful relationship between flow rate and pressure gradient (Siau 1995).

When Darcy's law is applied to gaseous flow, the expansion of gas and resulting changes in gradient throughout the specimen need be considered and can be rewritten as follows (Siau 1995):

$$k_g = -\frac{V}{t\,A\,dP/dL} \tag{2.6}$$

By applying the ideal gas law, Equation (2.6) produces Darcy's law for gases:

$$k_g = \frac{V\,L\,P}{t\,A\,\Delta P\,\overline{P}} \tag{2.7}$$

where, P is the pressure at which V is measured, $\Delta P = P_2 - P_1$, and $\overline{P} = (P_1 + P_2)/2$. P_1 and P_2 are the pressure at the inlet and outlet of the specimen.

Specific permeability or intrinsic permeability, K (m^3/m), is independent of the nature of fluid but depends on the geometry of the voids in a porous media.

$$K = k\,\eta \tag{2.8}$$

where η is the dynamic viscosity (Pa·sec). And k ($m^2 \cdot Pa^{-1} \cdot sec^{-1}$) is named as superficial permeability.

Darcy's law provides a convenient way of measuring permeability, but all interactions between the fluid and porous media are lumped into k; it does not reveal any relationship between k and the material properties. Since 1970s, researchers have been trying to understand the effects of different factors on the permeability of wood composites, which will be reviewed in the next sections.

2.3 Permeability of particleboard and MDF

The early work done on particleboard permeability in 1970s and 1980s was reviewed by Bolton and Humphrey (1994) and it revealed that it was significantly affected by board density, flow direction, and particle size: permeability decreased as the density increased, so did it as the particle size increased.

Humphrey and Bolton (1989) stated that the relationship between in-plane and transverse permeability was about 59:1. They also considered this ratio to be constant over the whole density range of particleboard.

Hata (1993) investigated the effects of particle geometry (length and thickness) and mat density on gas permeability of particleboard. The results indicated that: gas permeability decreased as the particle length and thickness increased. Increasing mat density was found to decrease gas permeability, in both transverse and in-plane permeability. Hata (1993) also developed empirical equations to predict gas permeability in two directions with particle geometry and compaction ratio:

$$k_{in} = 1110l - 4540w + 531450t + 700w \cdot l - 63300l \cdot t + 1.1\exp(15.42 - 7.32C) - 14252 \quad (2.9)$$

$$k_{tr} = 590l - 260w + 163460t - 20300l \cdot t + 1.14\exp(13.87 - 8.12C) - 4915 \quad (2.10)$$

where k_{in} and k_{tr} are permeability in the in-plane and transverse direction ($cm^2\ atm^{-1}\ s^{-1}$), l, t, w are the length, thickness and width of the particle (cm), C is the compaction ratio.

Haas *et al.* (1998) presented the transverse and in-plane permeability for fiberboard, particleboard and OSB. The permeability was measured on finished panels with a uniform density profile. The determination of permeability as a function of density was expressed as:

$$K = \exp\left(\frac{1}{a + b \cdot \rho + c/\ln\rho}\right) \quad (2.11)$$

where K is the specific permeability (m^2), ρ is the board density ($kg\ m^{-3}$), a,b, and c are coefficients related to wood element type, resin content and flow direction.

Based on the work of Sokunbi (1978) and Humphrey and Bolton (1989), Carvalho and Costa (1998) fitted an exponential curve to predict the transverse permeability of particleboard:

$$K_{tr} = 17.4 \times 10^{-12} \exp(-8.06 \times 10^{-3} \rho) \quad (2.12)$$

Garcia and Cloutier (2005) presented the results obtained for transverse gas permeability as a function of panel density yielding R^2 of 0.99:

$$\log(K) = -6\times10^{-6}\times\rho^2 + 0.0048\times\rho - 12.93 \qquad (2.13)$$

The panels measured by Garcia and Cloutier (2005) had a reasonably homogeneous density profile. Gas permeability decreased with an increase in panel density. The permeability values were in the same order of magnitude as those published by Hata *et al.* (1993).

Thoemen and Klueppel (2008) compared the transverse and in-plane permeability for two kinds of particle mat and one kind of MDF mat. The transverse and in-plane permeability of particle and MDF mats showed little difference at low densities, while the in-plane permeability exceeded the transverse permeability by one-order of magnitude. MDF mats exhibited a lower permeability values for a given density. The results indicated that wood element type and its characteristics also affected the mat permeability except for mat density and flow direction.

2.4 Permeability of veneer- and strand-based wood composites

Haas *et al.* (1998) provided the coefficients in Equation 2.11 for a resin content of 5%. The in-plane permeability, including in parallel and perpendicular to strand orientation, and transverse directions, can be calculated and are plot in Figure 2.1.

$$K_{in\_pa} = \exp\left(1/\left(0.049 - 3.22\times10^{-6}\times\rho - 0.540/\ln\rho\right)\right) \qquad (2.14)$$

$$K_{in\_per} = \exp\left(1/\left(0.049 - 2.41\times10^{-6}\times\rho - 0.540/\ln\rho\right)\right) \qquad (2.15)$$

$$K_{tr} = \exp\left(1/\left(0.043 - 2.79\times10^{-6}\times\rho - 0.481/\ln\rho\right)\right) \qquad (2.16)$$

where K_{in_pa} is the in-plane permeability in the direction parallel to strand orientation, K_{in_per} is the in-plane permeability in the direction perpendicular to strand orientation, and K_{tr} is the transverse permeability.

The permeability values in parallel and perpendicular directions were in the same order of magnitude in spite of the difference increasing with density. The in-plane permeability was about 10 times the transverse permeability.

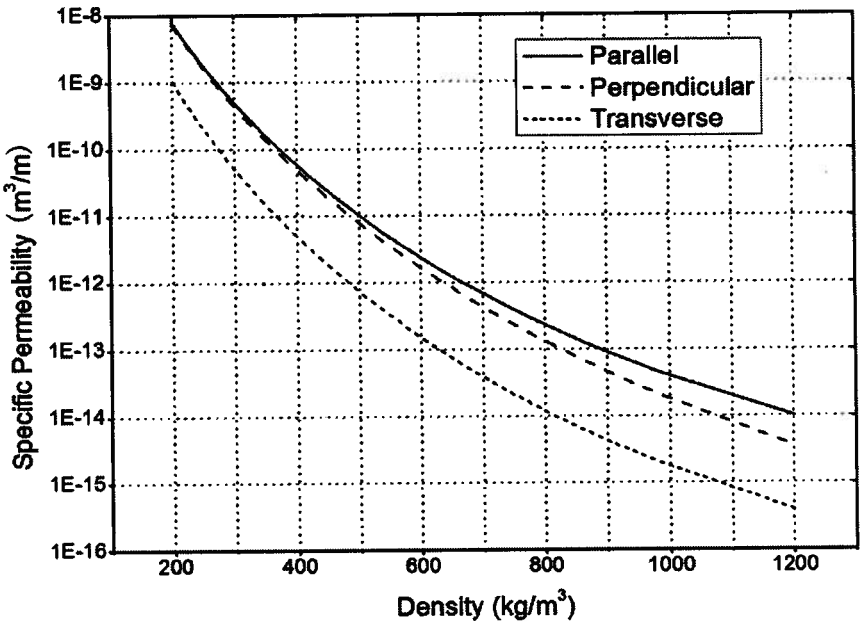

Figure 2.1: Predictions for in-plane parallel and perpendicular permeability and transverse permeability of OSB based on Haas 1998.

Hood (2004) and Hood *et al.* (2005) investigated the effects of flake thickness, flake orientation, and mat density of OSB on gas permeability through transverse and in-plane of the panel. No adhesive was used in the formation of the mats, with the exception of the highest density (800 kg/m^3) mats. The results indicated that: both transverse and in-plane permeability decreased rapidly as the compaction ratio increased; transverse and in-plane permeability were higher for mat composed of thicker flakes. Empirical equations were also developed for three principle directions:

$$k_{tr} = \exp(-16.9 - 0.896C - 1.23C^3 + 204t^2) \qquad (2.17)$$

$$k_{in\_pa} = \exp(-13.4 - 0.486C^5 + 34.0t) \qquad (2.18)$$

$$k_{in\_per} = \exp(-12.4 - 0.459C^5 + 14.1t) \qquad (2.19)$$

where k_{tr}, k_{in_pa}, and k_{in_per} are superficial permeability (m^{-2} Pa^{-1} s^{-1}) in transverse, in-plane parallel to strand orientation, and in-plane perpendicular to strand orientation respectively; C is compaction ratio, and t is flake thickness (cm).

With the assumption that the mat permeability was due to the voids between strands instead of those inside strands, Dai *et al* (2005) developed a model for mat permeability

based on the classic Carman-Kozeny theory and the mat structure, which linked the mat permeability to mat porosity and strand dimensions.

$$K = \frac{t_e^2 \phi_b^3}{\tau'(1-\phi_b)^2} \qquad (2.20)$$

where K is the specific permeability (m^2), ϕ_b is the between-strand porosity, t_e is the effective strand thickness, and τ' is the tortuosity constant, which is determined for best fit with experimental data. The assumption was validated by comparing the transverse permeability of OSB and the perpendicular-to-grain permeability of aspen. The wood permeability is lower by one order of magnitude. It implied that the voids inside strands contributed little to the overall flow transversely passing through the board.

The model predictions in Equation 2.20 agreed with the experimental data well. The experimental results indicated that permeability was more sensitive to small strands than large strands. A similar trend also appeared in particleboard, as reported by Thoemen and Klueppel (2008). And strand length and width had diminished effects on permeability at low density range.

Fakhri *et al.* (2006a, b) examined the effects of density and core fines content on the transverse permeability of OSB. The core permeability K_{core} decreased with increasing density and it increased exponentially with fine content below 75% at each density level, as shown in Figure 2.2 and 2.3.

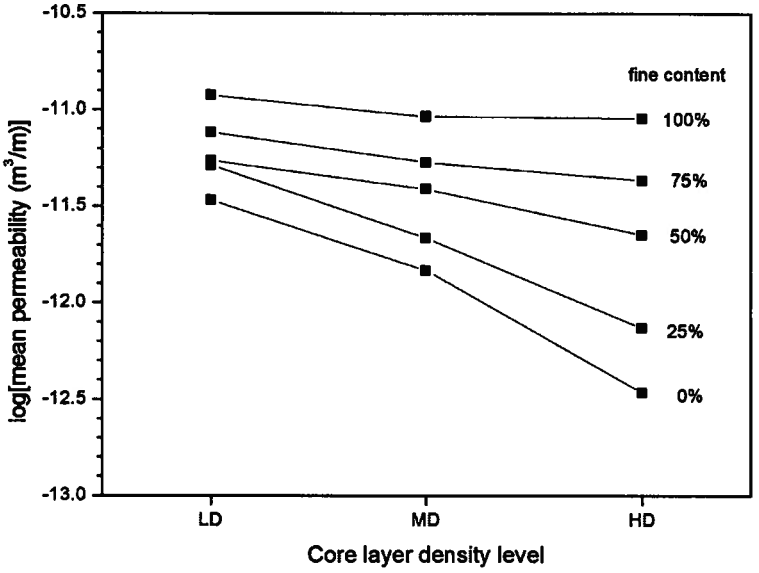

Figure 2.2: The relationship between average logK and core target density: LD=low density, MD=medium density, and HD=high density (adapted from Fakhri et al. 2006a).

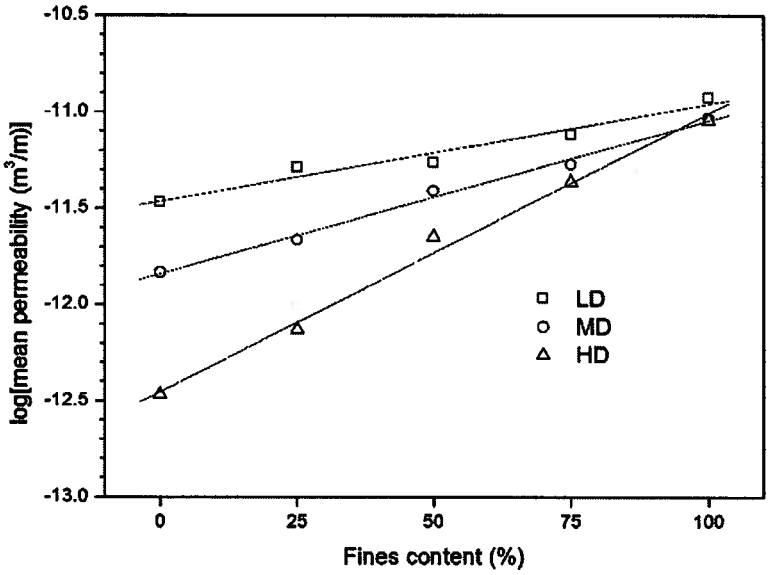

Figure 2.3: Log-linear fits to mean core permeability as a function of fines content: LD=low density, MD=medium density, and HD=high density (adapted from Fakhri et al. 2006a).

A model was developed by Fakhri *et al.* (2006b) to characterize the permeability of OSB as a function of fines content and density. Strands and fines in the core of the board are considered to lie either in a series configuration or in a parallel configuration. With the

experimental data, the hypothesized permeability of series and parallel configuration were obtained with regression. A coefficient α was employed to determine the contribution of each model to the overall system permeability.

$$K_{system} = \alpha K_{series} + (1-\alpha) K_{parallel} \qquad (2.21)$$

Wang *et al.* (2006) investigated the transverse air permeability of trembling aspen (*Populus tremuloides*) veneer and phenol formaldehyde gluelines, as well as aspen plywood and randomly oriented strandboard (ROSB). For veneer-based panels, the compression ratio was the most important factor affecting panel permeability, followed by the sapwood/heartwood composition and gluelines. The permeability of the sapwood veneer panels was approximately four-fold higher than that of the heartwood. The glueline permeability decreased during glue curing. The permeability of the cured plywood PF glue films decreased with increasing glue-spreading level. At the same density, veneer panels had much lower permeability than ROSB. Moreover, the permeability of veneer panels tended to decrease with density more rapidly than that of ROSB.

Similar to the model used by Fakhri *et al.* (2006b), the glued two-ply veneer panel was considered as a multi-layer laminate comprising two veneer plies and one glue film, which arranged in series (Wang *et al.* 2006). According to the theory of Dullien (1992), the overall permeability was calculated as:

$$\frac{t}{K} = \frac{t_{veneer1}}{K_{veneer1}} + \frac{t_{veneer2}}{K_{veneer2}} + \frac{t_{gluefilm}}{K_{gluefilm}} \qquad (2.22)$$

where K is the permeability of glued two-ply veneer panel, $K_{veneer1}$ and $K_{veneer2}$ are the permeability of veneer plies 1 and 2, t is the total thickness of the veneer panel, $t_{veneer1}$ and $t_{veneer2}$ are the average thickness of the glue film, $K_{gluefilm}$ is the permeability of the glue film. The results showed that the predictions had an error of less than 15%.

2.5 Microscopic investigation on the compression of wood and wood composites

Since 1970s microscopic and advanced imaging techniques such as high magnification light microscope, scanning electron microscope (SEM) and X-ray tomography, have been used to study the structure of porous materials, e.g. concrete, soil, and rocks (Blair *et al.* 1996, Schaap and Lebron 2001, Flannery *et al.* 1987, and Lu *et al.* 2006). The microscopic techniques also have been applied to characterize the wood mechanical and physical properties.

Tabarsa and Chui (2000) used the microscope to analyze the stress-strain response of white spruce (*Picea glauca*) under radical compression. The results indicated: the elastic and plastic parts of the stress-strain response for white spruce under radial compression were primarily controlled by earlywood, and the densification region was largely an elastic response of the latewood. The cell wall collapse was due to the formation of plastic hinges rather than bucking of the cell wall.

In the later work Tabarsa and Chui (2001) studied the microscopic behavior of different wood species under transverse compression. It was found that the deformations in hardwoods and softwoods were not uniformly distributed throughout a growth ring. For softwoods, deformation was inversely proportional to the thickness of cell walls, while in hardwoods first failure initiated in the largest vessels surrounded by thin-walled paratracheal parenchyma cells.

Muller *et al.* (2003) used SEM to investigate the cell deformation of different wood species loaded perpendicular to grain. It was revealed that the wood species had different compression behavior mechanics according to their cell structures, e.g., the radial compression of white spruce was limited by the critical Euler bucking load of only a few cells closely behind the ring boarder, while the behavior of oak was determined by the bucking of the earlywood vessels and vasicentric tissue.

The earliest work using microscopic techniques to characterize wood composites includes Geimer *et al* (1985). They investigated the cell structure damage of Douglas-fir flakeboard induced by transverse compression during the hot-pressing. They concluded

the following: (i) earlywood tracheids were crushed more than latewood due to the lower density of earlywood; (ii) entire rows of tracheids failed at one time; and (iii) cell wall failures were the result of buckling and bending.

To obtain a better understanding of material behavior during the manufacture of wood-based composites, Kultikova (1999) evaluated the effect of densification treatments on the changes in the structure of yellow-poplar and loblolly-pine. The results proved that the temperature alone did not change the geometry of wood structure. But a difference was noted in the type of failure between the two species: the earlywood tracheids of loblolly-pine were crushed more considerably than latewood areas as a result of the abrupt transition between earlywood and latewood, which was similar to that observed by Geimer *et al.* (1985) in Douglas-fir; for yellow-poplar, the distribution of compression throughout the section was more uniform, although earlywood cells showed more structural damage than latewood.

Several research groups have used X-ray tomography in an attempt to quantify the void geometry of wood composites, e.g. Sugimori and Lam (1999), and Zhang *et al.* (2005). Sugimori and Lam (1999) provided a method to analyze the macro-void distribution in strand-based wood composites. The X-ray images were converted to the three-dimensional measurements of macro-voids.

Zhang *et al.* (2005) did a similar work which provided a 2D and 3D visualization of void structure in OSB and investigated the effects of mat density on void ratio. They found that over a large density range, voids in OSB decreased exponentially with increasing in density. It also inspected different threshold levels and pixel values of images: void ratio increased with an increased threshold level, so did it when pixel value increased.

2.6 Summary

The general concept of permeability and its significant effect on hot-pressing process in wood composites manufacture were presented. Previous research has investigated the permeability of several kinds of wood composites. However, no published work has addressed the in-plane permeability of oriented strand-based, resinated wood composites, and the void structure development during densification.

In Chapters 3 and 4 the in-plane permeability of oriented strand-based composites were measured and discussed, and in Chapter 5 the void structure changes were investigated on a microscopic level.

3 Materials and Methods

3.1 Sample preparation

A series of laboratory made panels were pressed over a range of different densities. In a commercial hot-pressing process, the final density of OSB ranges from 500 to 800 kg/m^3. Below about 450 kg/m^3, panel permeability changes little as the density increases (Hood *et al.* 2006). Therefore, the targeted panel densities were chosen as 450, 550, 625, 700 and 800 kg/m^3; 4 replicates were made for each density for a total of 20 panels.

3.1.1 Materials and mat composition

Aspen (*Populus tremuloides*) strands were supplied by Ainsworth Lumber Co. Ltd., Grande Prairie, AB, Canada. They were 150-180 mm (6" - 7") in length, 25 mm (1") in width, and 1 mm in thickness. The nominal panel dimensions were 559 mm long by 305 mm wide by 32 mm thick (22"×12"×1.25"). No wax was used in order to minimize the additional confounding effects from its presence. The resin used for panel production was liquid phenol formaldehyde resin with a solid content of 59% (Cascophen OSF-59FLM, made by Hexion Canada).

Table 3.1: Mass content required to produce one board for 450kg/m^3.

Description	Value	Units
Board length	559	mm
Board width	305	mm
Board thickness	32	mm
Board volume	5.41×10^{-3}	m^3
Board moisture content	1.5	%wt of od board
Board resin content	6	%wt of od board
Board wax content	0	%wt of od board
Resin solids content	59	%wt
Shipping density	450	kg/m^3
Furnish moisture content	9	%wt of od furnish
Board weight (wet)	2.434	kg
Board weight (od)	2.398	kg
Furnish weight (od)	2.254	kg
1 Furnish weight	2.457	kg
Resin weight (od)	0.144	kg
2 Resin (wet)	0.244	kg
1+2 Resinated furnish weight	2.700	kg

* od: oven dried

3.1.2 Resination

The strands and resin were blended in a 1.50m (5ft) in diameter and 0.61m (2ft) in depth drum blender (as shown in Figure 3.2). The process of blending strands was as follows: the required mass of strands and resin for each board were weighed. The strands were placed in the blender, and the resin was sprayed on the strands using a nozzle with an air pressure of about 200 – 350 kPa (30-50 psi). When the strands were resinated, the blender was rotating at a rate of 100 rpm and the resination lasted for 7 minutes for each batch. Each time the blender was loaded with the materials for one panel only.

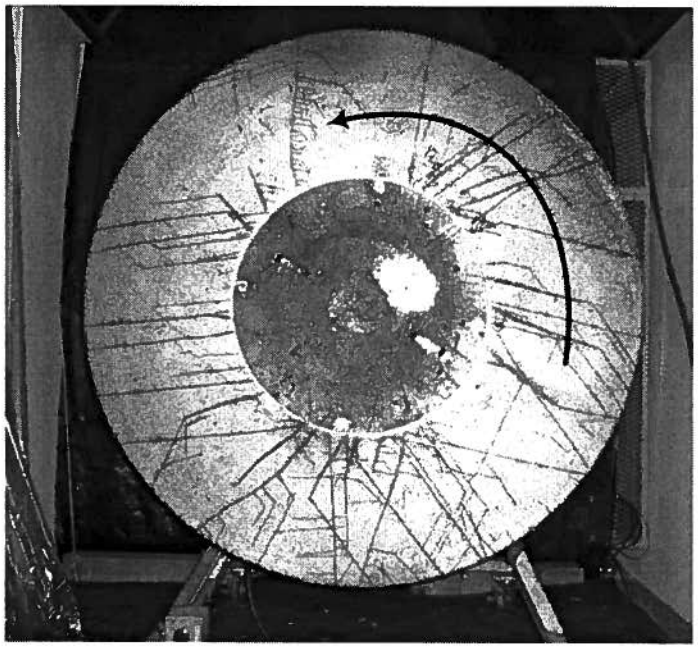

Figure 3.1: The blender used to resinate the strands: the arrow indicates the rotating direction.

After each batch was finished, the blender was left for 10 minutes to permit the resin droplets to settle before it was opened. The resinated strands could then be used for the mat formation process.

3.1.3 Mat formation

The resinated strands were handpicked to have a length of 100–180 mm (4"-7"), width of 20-40 mm (0.75"-1.5") and thickness of 1mm. Examples of accepted strands are shown in Figure 3.2a-c and residuals in Figure 3.2d.

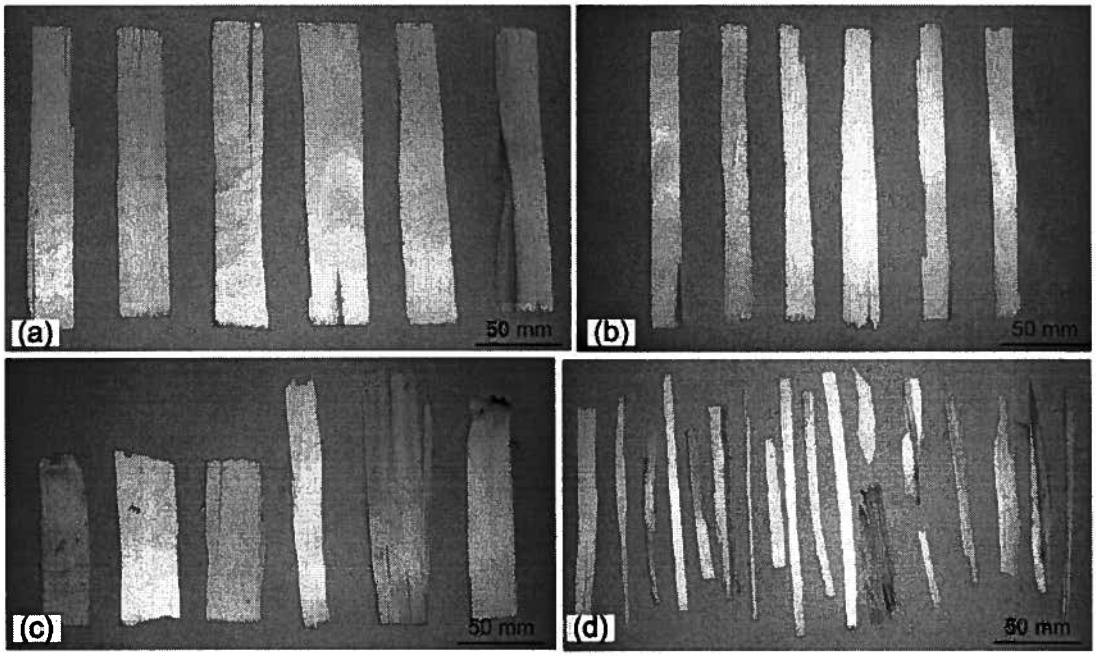

Figure 3.2: Type of strands used for mat formation: (a) long and wide strands, (b) long and narrow strands, (c) short strands; (d) residual strands after selection.

Selected strands were hand formed to assure an appropriate strand orientation and even mass distribution. A typical formed mat is shown in Figure 3.3. To eliminate the effects of moisture content changes, the mat was formed and pressed on the same day as the batch of strands was resinated.

Figure 3.3: A typical hand formed mat.

3.1.4 Hot-pressing process

The purpose of hot-pressing was to manufacture panels with uniform vertical density profile (VDP) that fall into the targeted density range. The formed mats were pressed in a 762 mm×762 mm (30"×30") Pathex press equipped in a PRESSMAN control system. Fifteen preliminary panels were made in order to determine an appropriate press cycle. The target density range was targeted to within ±30 kg/m^3 at 1.5% moisture content.

The pressing cycle was as follows: pre-heat press platens to 50°C, place mat into press, press the mat for 40 minutes at 200°C, and then removed from press, as shown in Table 3.2.

Table 3.2: Press schedule for panels with densities of 450-700 kg/m^3.

Segment	Control	Set Point (mm)	Segment Time (s)	End Condition
1	Fast Position	80.01	2	Position<=80.01
2	Position	50.01	5	
3	Position	40.00	5	
4	Position	31.80	20	
5	Position	31.80	20	
6	Position	31.80	400	
7	Position	31.80	2000	
8	Position	31.80	10	
9	Position	150.01	5	

The 800kg/m^3 test panels blew at the end of pressing when this press cycle was applied; inspection of the core gas pressure showed that it was very high, about 860 kPa, at the end of the press cycle. Increasing the pressing time from 40 to 70 min and decreasing the pressing temperature to 180°C, reduced the gas pressure at the end of press to 100 kPa and eliminated any further blows.

The PRESSMAN control system also recorded the mat thickness, mat pressure, core temperature, and gas pressure as a function of time, as shown in Figure 3.4.

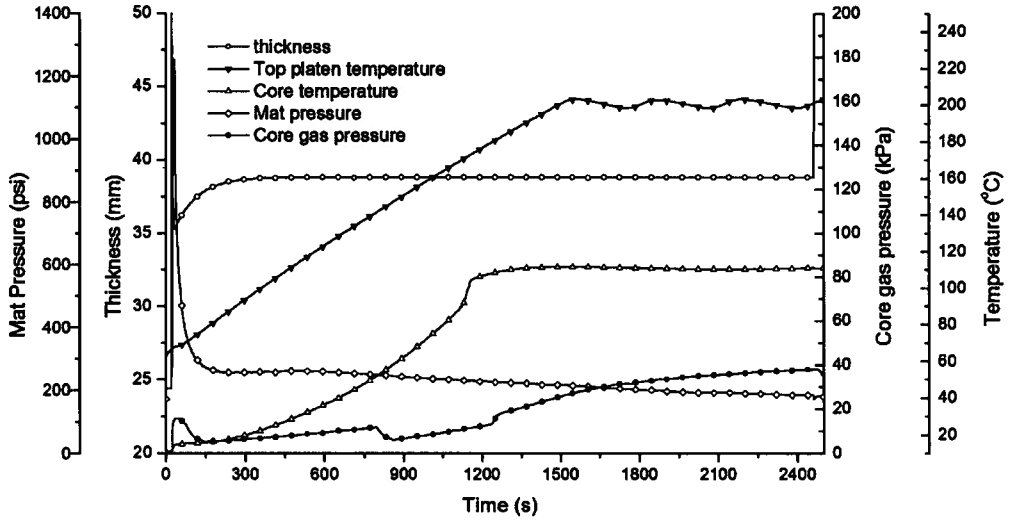

Figure 3.4: A typical press cycle: mat thickness, platen temperature, mat pressure, core gas pressure, and core temperature as a function of time.

After the hot-pressing process was over, the panel was taken out of the press. Samples of the finished boards are shown in Figure 3.5.

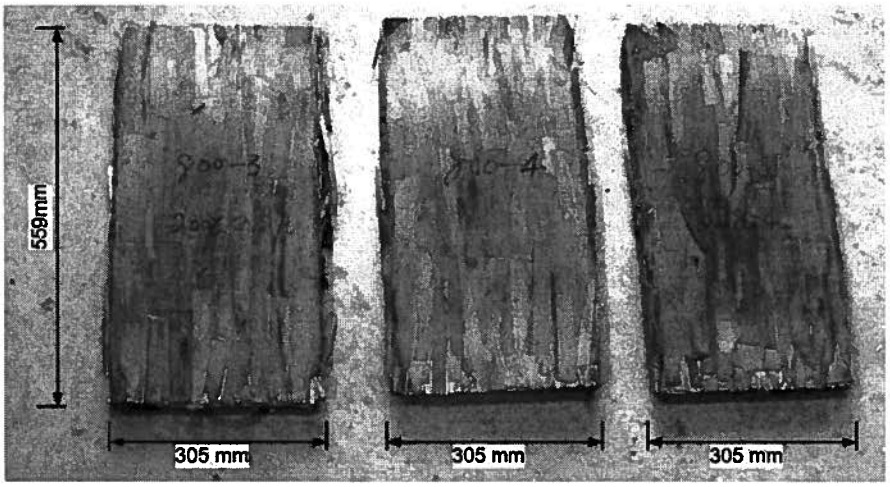

Figure 3.5: Samples of finished panels.

3.1.5 Sample preparation

Finished panels were 559 mm by 305 mm by 32 mm and were cut into one 203 mm by 203 mm (8" by 8") sample for permeability measurement and eight 51 mm by 51 mm (2"

by 2") samples for VDP tests, as shown in Figure 3.6. The specimens are shown in Figure 3.7. The sizes were determined according to the requirement of measuring apparatus.

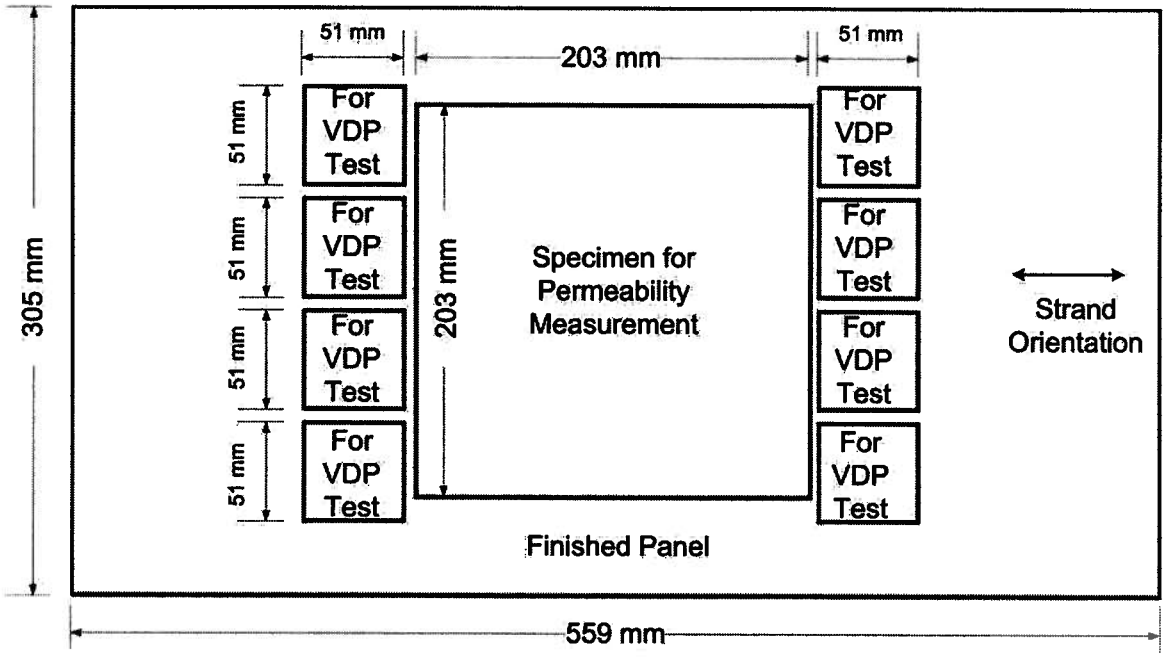

Figure 3.6: Cutting pattern.

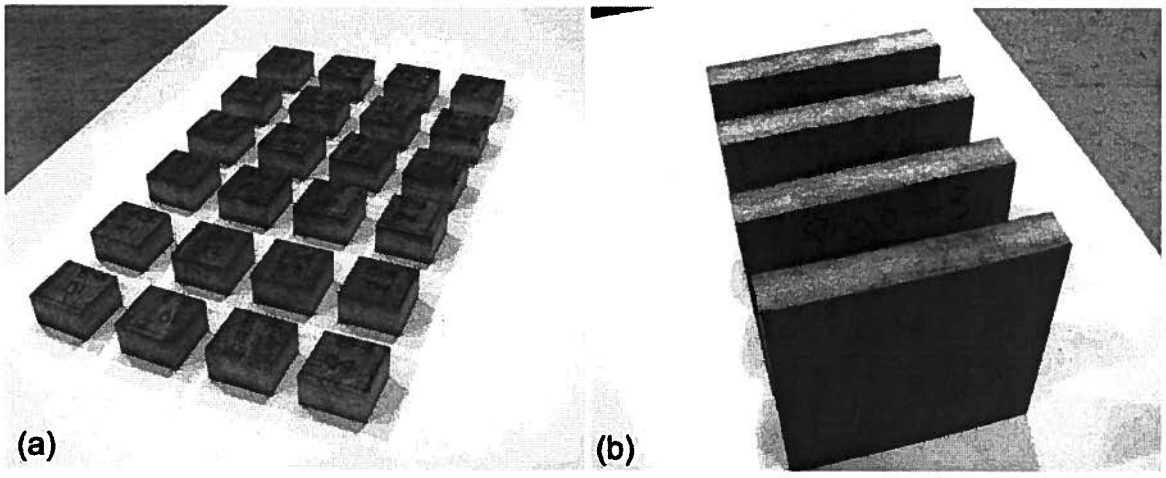

Figure 3.7: Specimens cut from finished panels: (a) 51 mm by 51 mm samples for VDP test, (b) 203 mm by 203 mm samples for permeability tests.

After cutting, all the specimens were conditioned at 20°C and 65% relative humidity for more than 15 days before they were tested.

3.2 Experimental design

The panel density and flow direction were factors examined in this study. The panel preparation process below was used to reduce the variability caused by density variation: all the mats had the same hot-pressing cycle (except the 800 kg/m^3 ones); the strands were handpicked and mats hand formed by the same person to reduce the variability of strand size and in-plane density distribution; the hot-pressing cycle introduced in the previous section ensured that panels had a uniform vertical density profile. The in-plane density distribution and VDP were measured after the boards were pressed.

The experiment consisted of 5 density levels, with 4 replicates for each density, for a total of 20 specimens. The in-plane permeability of each specimen was measured in three directions: parallel, perpendicular, and 45° to the strand orientation.

3.3 Apparatus

The apparatus to measure the in-plane permeability of thick wood composites was composed of two parts: a specimen holder that could seal the specimen faces and edges to enable the air to flow in the desired direction, and a permeability measurement system that could be connected with the specimen holder, and record the air flow to calculate the specific permeability.

3.3.1 Permeability specimen holder design and sealing

Aluminum specimen holders were constructed for permeability measurements and were composed of six individual plates: top and bottom face-plates, two side-plates and two end-plates. Face-braces were also designed to have an even pressure distribution and prevent any bending of top or bottom plates. Two different sets of specimen holders were designed: one for large specimens, 203 mm by 203 mm, and one for small specimens, 127 mm by 127 mm in order to measure air flow in different directions. The original design used bolts to assemble plates together and was sealed with rubber laminates and O-rings, as shown in Figure 3.8. Holes were drilled in the end plates and a hose connection inserted to connect a tube to permeability measurement apparatus.

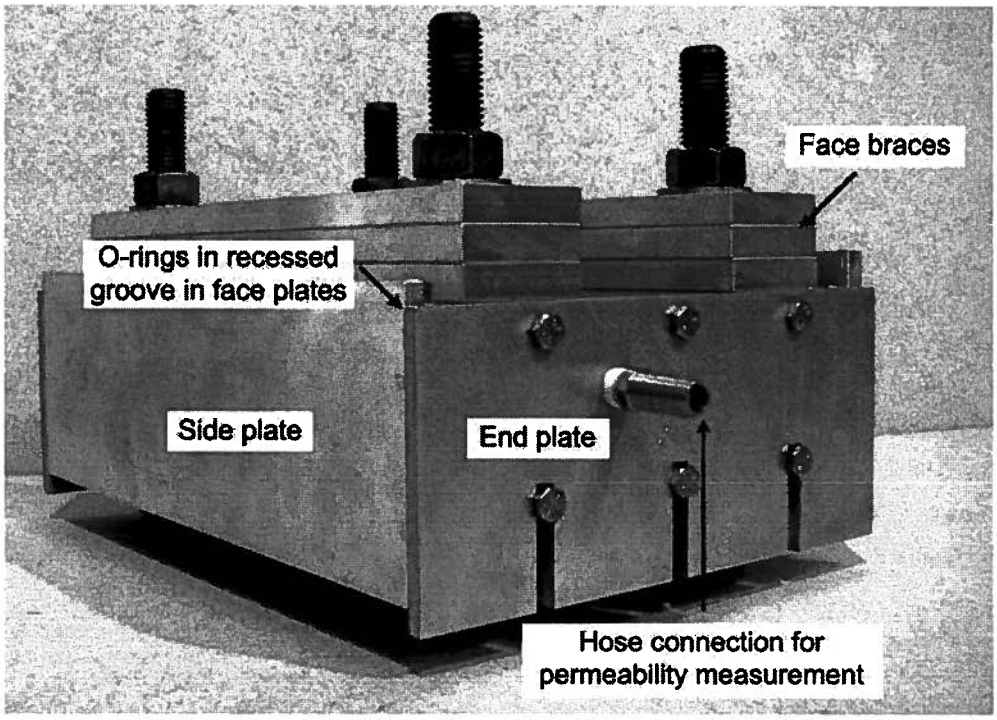

Figure 3.8: Specimen holder assembling of original design (note that the face-plates are concealed by the side- and end-plates).

Rubber laminates and O-rings were tried first, which led to significant leakage from the contact between plates. After numerous attempts to get the specimen holder to seal to the o-rings, the approach was abandoned. The next step was tried to glue the whole specimen holder and samples together using a latex sealing adhesive. Latex requires at least 24 hours to be totally cured with assuming that there is adequate exposure of the adhesive to air so that water within the sealer can evaporate. Unfortunately the enclosed environment of the specimen holder prevented the water from evaporation and the latex did not cure.

In order to get around the solvent loss issues with the latex adhesive, a catalyzed epoxy system was tried. It did cure overnight, but when tested was also found to leak even after three additional applications of epoxy. An issue both the latex and the epoxy had was that it was difficult to disassemble the specimen holder afterwards; the latex had to be carefully cut apart with a thin blade and the epoxy heated.

Finally, hot-melt glue was tried. The thought here was that disassembly would be much easier as the whole specimen holder and sample could be placed on the hot-plate and

heated to above the melting temperature of the glue. Hot-melt glue turned out to be a much better sealant. The one used here was Scotch-Weld™ 3738AE manufactured by 3M (Minnesota, USA). It contains a mixture of ethylene-vinyl acetate polymer (24937-78-8), hydrocarbon resin (68478-07-9), synthetic rosin resin (undeclared), and polyolefin wax (mixture). Its ball and ring melting point is 86°C (186°F), and the adhesive fails at 54°C (130°F). The viscosity is 2.875 Pa·s (2875cps) at 191°C (375°F).

The setting process involves the heat-induced softening of a thermoplastic resin rather than vapor loss, which leads to a faster setting (the specimen holder would cool in about 15 minutes when placed on a water-cooled plate) and does not require the use of bolts. After measurement, the specimen holder was then disassembled by heating on a hot plate. The design of a new mold, based on the use of hot-melt exclusively, is shown in Figure 3.9.

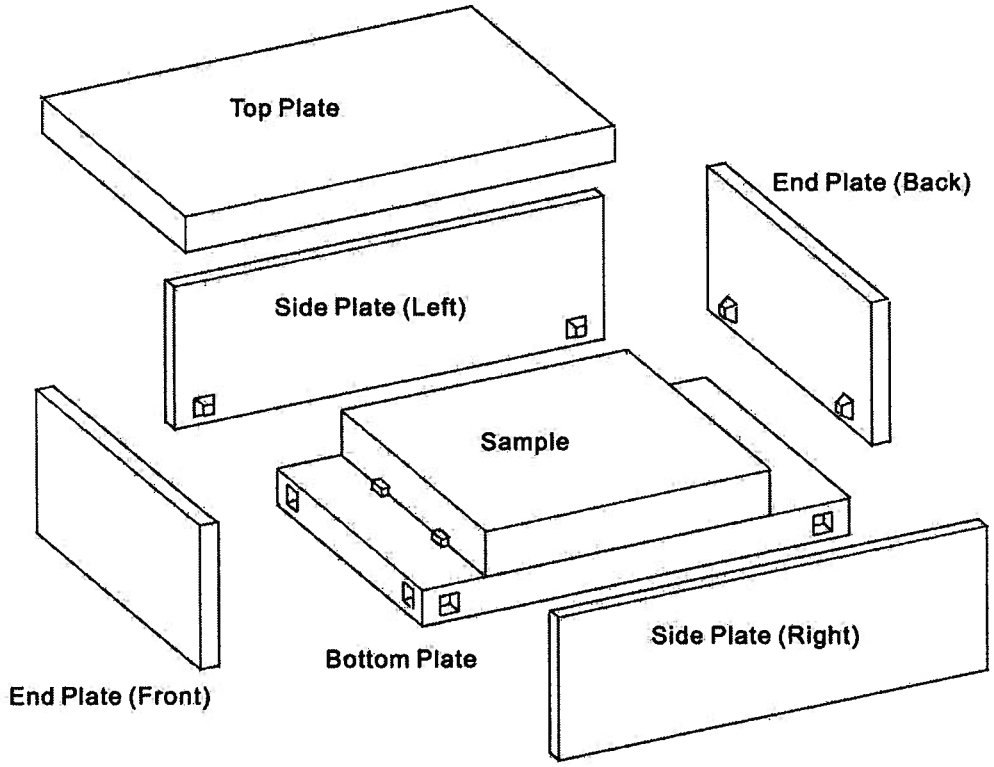

Figure 3.9: Design of the permeability measuring specimen holder.

Due to cost constraints, the new specimen holders were not built. Rather the slots and holes in the original specimen holders were sealed. Holes were also drilled into the two

end plates to connect to the permeability measurement apparatus. The assembly sequence for containing a specimen was shown in Figure 3.10.

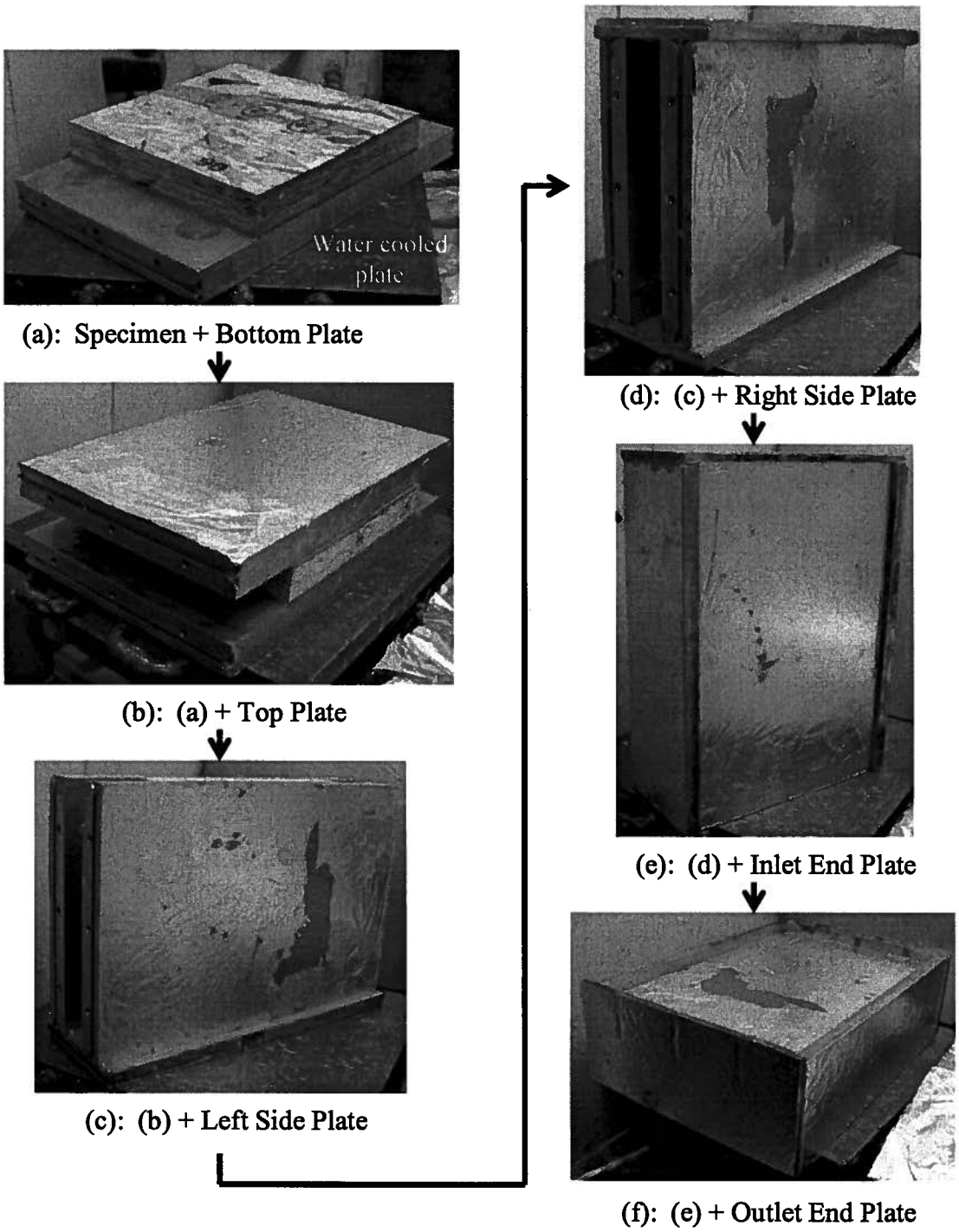

Figure 3.10: Assembly of the permeability measuring specimen holder.

3.3.2 Permeability measurement apparatus

After the specimen holder was cooled to room temperature it was connected to the permeability measurement apparatus which was developed on the theory of Siau (1995). The apparatus was designed by the falling water displacement method, as shown in Figure 3.11.

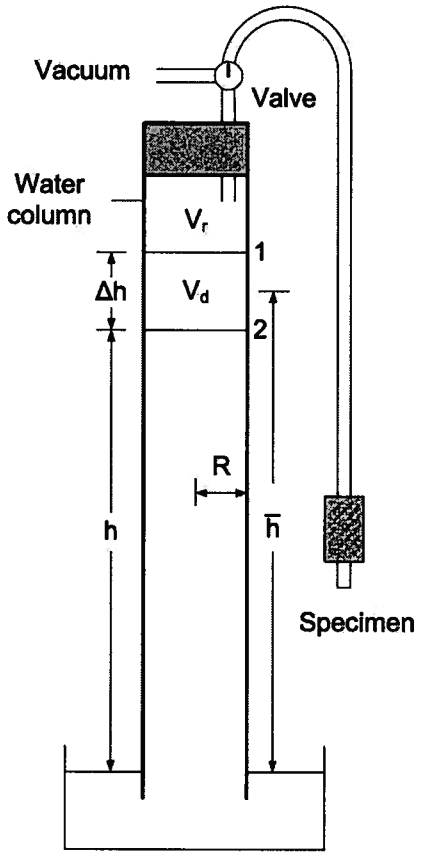

Figure 3.11: Schematic diagram of air permeability measurement apparatus (modified from Siau, 1995).

The permeability apparatus is shown in Figure 3.12. Four tubes with different diameters were assembled which could fulfill the specific permeability measurement ranging from 10^{-16} to 10^{-10} m^3/m. The air outlet end was blocked initially to test for any air leakage in the system, which could be revealed by the motion of the water level. If the sealing was sufficient, the outlet end was opened to measure permeability.

There were two main issues associated with this system that had to be addressed.

1. Determining whether there was unaccounted air flow occurring through any spaces between specimen holder plates and specimen surfaces.
2. Determining whether the hot-melt glue was seeping into the specimen which could reduce the cross-sectional area for air flow used in the permeability calculation.

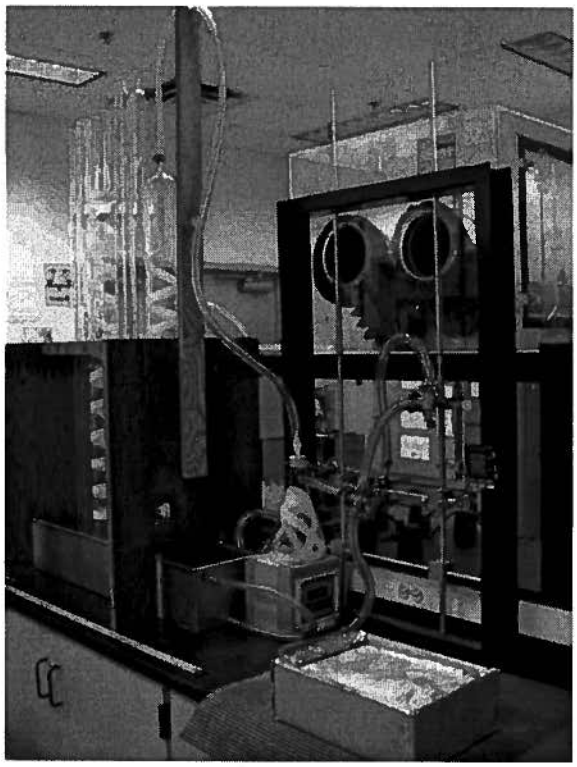

Figure 3.12: Permeability measuring apparatus.

To address the first problem, an impermeable plastic blank of the same dimensions as the wood specimens was tested in the system with the outlet end open and the level of the water in the tube observed over a period of time. The water level remained stable indicating no gas passing through spaces between plates and specimen surfaces and indicated that the hot-melt glue completely sealed the specimen. The second concern was addressed by cutting cross sections from specimens and then examined with a hand lens. It was found that almost all the hot-melt glue stayed on the sample surface and any amounts absorbing into the specimen surface were negligible.

3.4 Permeability measurements

Equation (3.1) modified from Darcy's law was used to calculate superficial permeability values (Siau, 1995):

$$k_g = \frac{152VCL(P_a - \bar{h}/13.6)}{tA(\bar{h}/13.6)(2P_a - \bar{h}/13.6)} \qquad (3.1)$$

where L is the length of specimen in the direction of flow (mm), P_a is the atmosphere pressure (mm of mercury), $\bar{h}$ is the average height of water over surface of reservoir during measurement (mm), t is the time of measured flow (s), A is the cross-section area of specimen perpendicular to flow direction (mm^3), Δh is the change in the height of water during the period of measurement (mm), R is the radius of measuring tube (mm), and V_r is the total volume above the original water height (mm^3).

V is the volume of liquid flowing through specimen (mm^3):

$$V = \pi R^2 \Delta h \qquad (3.2)$$

C is the correction factor when V_r is a significant portion of the total volume of the system:

$$C = 1 + \frac{V_r(\Delta h/13.6)}{V(P_a - \bar{h}/13.6)} \qquad (3.3)$$

The specific permeability, independent of the measuring fluid, is calculated based on Equation 2.8. The dynamic viscosity is chosen as 1.846×10^{-5} Pa·sec for standard air at 25°C (Denny 1995).

Permeability in the direction parallel to strand alignment was measured first. Then the two sealed sides of specimens were trimmed off to have a clean cross section for tests along the perpendicular direction. Finally, a 127.0 mm by 127.0 mm by 31.8 mm specimen was cut along directions that had 45° angle to the strand orientation. The sequence is shown schematically in Figure 3.13. The light lines and arrows inside the specumen indicate the direction of strand alignments.

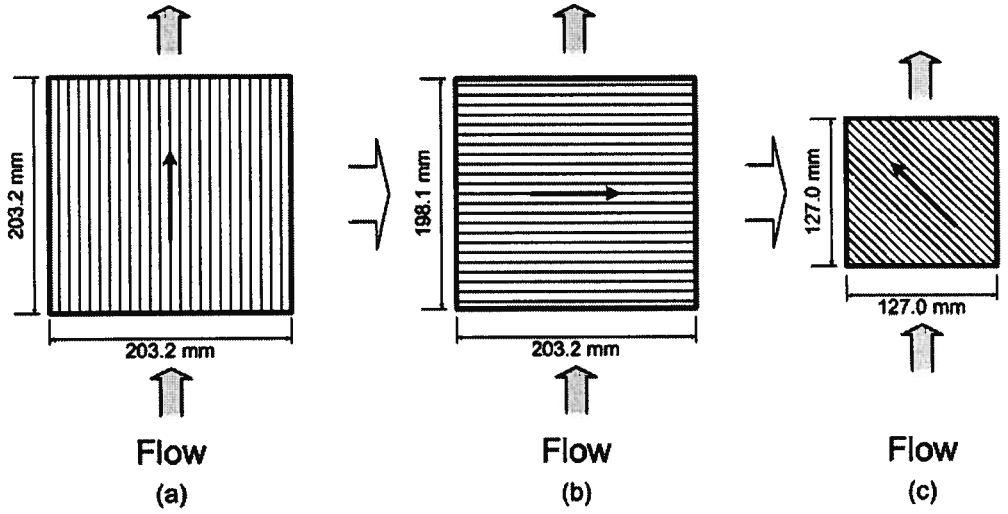

Figure 3.13: Sample dimensions for the measurement in different directions: (a) parallel, (b) perpendicular, and (c) 45°. The arrows in the samples indicate directions of strand orientation.

3.5 VDP test

VDP tests were performed on 50.8 mm by 50.8 mm by 31.8 mm pieces with Quintek Measurement System (Model QDP-01X) and recorded by QMS Density Profile System – v1.30 (located at FPInnovations - Forintek Division, Vancouver). The system generates analytic X-ray beam and measures its attenuation transmitted through the samples. During the scanning, the X-ray beam, parallel to the plane of the specimen, passes across the thickness of the panel.

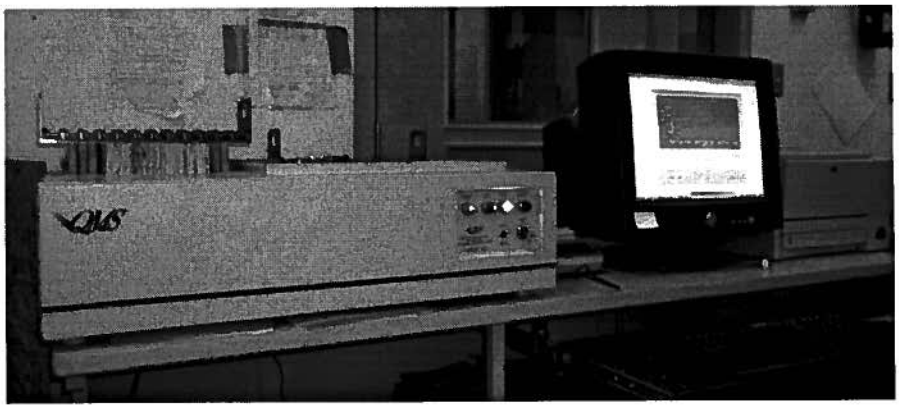

Figure 3.14: Quintek measurement system and QMS density profile system.

3.6 In-plane density distribution measurement

The purpose of this measurement was to test whether the density in-plane was evenly distributed, which was the aim of the hand formation process.

The 203 mm by 203 mm by 32 mm (8" by 8" by 1.25") specimen was cut into 16 blocks with a size of 51 mm by 51 mm by 32 mm (2" by 2" by 1.25"). Then the density was measured in the QMS Density Profile System. The density variance and distribution of the blocks were obtained. Once the specimen was cut it could not be utilized in the permeability measurement, therefore, only two test panels were investigated for the in-plane density distribution.

3.7 Data analysis

The calculation of permeability was conducted and then saved on Excel spreadsheets. The data was imported into MINITAB software (version 15.1.1.0) for all the statistical analysis. A 95% confidence level was used for the significance test and α=0.05 was used for Tukey's HSD test. An empirical equation was developed by performing linear and polynomial regressions on the data obtained in each direction. The R^2 was compared and the equation with the highest R^2 was chosen.

4 Results and Discussions

4.1 VDP test results

The VDPs for five representative samples are shown below. To make it easier to read, the profiles for 550kg/m^3 and 700kg/m^3 were plotted separately from the other three boards, as shown in Figures 4.1 and 4.2.

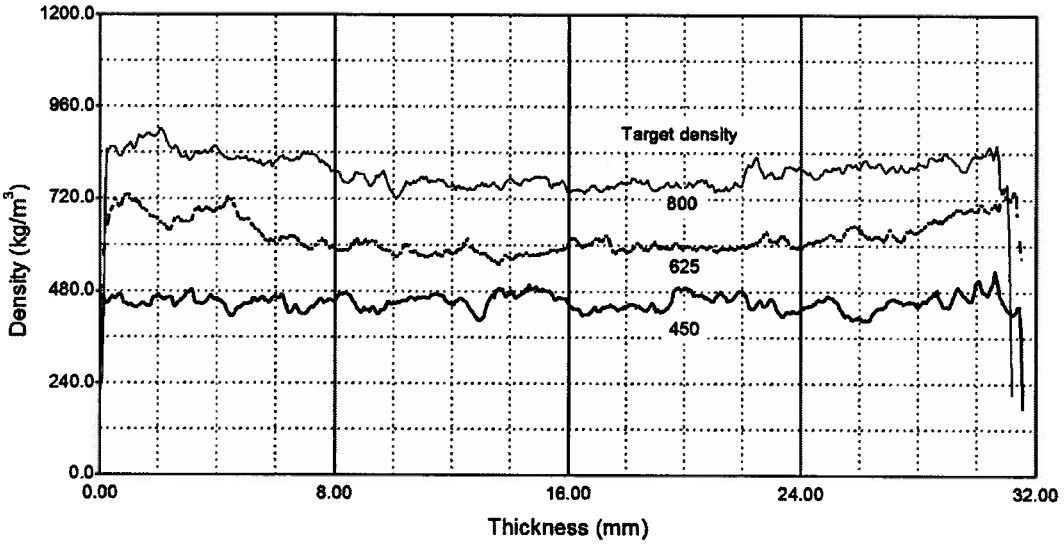

Figure 4.1: VDP of laboratory made boards with target densities: 450, 625, 800 kg/m^3.

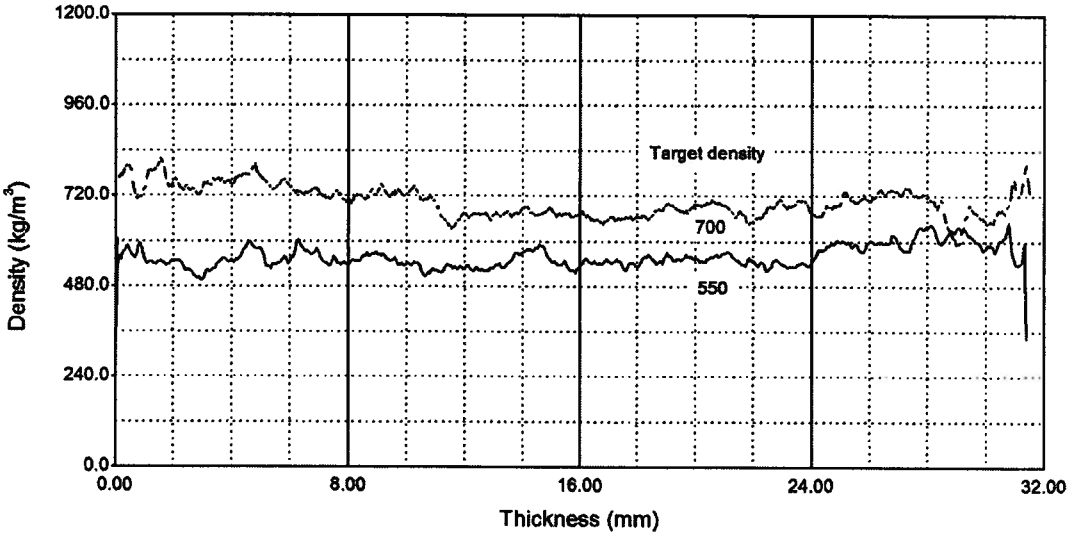

Figure 4.2: VDP of laboratory made boards with target densities: 550, 700 kg/m^3.

The figures indicated that panels used in the experiments had a reasonably uniform vertical density profile, confirming that the measured permeability value of a sample was for a uniform density across the face and core layers rather than a combination of different core and surface densities.

4.2 In-plane density distribution test

For comparison all the densities were computed at moisture content of 1.5% because the target density was set at this level. For a target density of 550 kg/m^3, the 16 specimens cut from one test board had an average density of 550.8 kg/m^3. The 95% confidence interval was (531.6, 568.5) kg/m^3, which fell into the target density range (530, 570) kg/m^3.

For another test board, the average density was 444.9 kg/m^3 for a target density 450 kg/m^3. And the 95% confidence interval was (434.1, 455.8) kg/m^3, which was also in the target density range (420, 470) kg/m^3.

From the results, it was concluded that the hand forming and hot-pressing process produced panels with even in-plane density distribution. In combination with the VDP test results, it was proved that the density measured in this experiment well represented the board property. They were reliable for further analysis and the direct relationship between density and permeability could be established.

4.3 Results and discussions

The original permeability values were not normally distributed (p<0.010), as such a logarithm transformation was applied and the transformed permeability values were found to be normally distributed (p>0.05). All of the statistical analyses below were performed on the transformed data. The density values used here were all oven-dried samples since moisture content was not in the scope of this research.

The measurements are shown in Figure 4.3, in which each point represents one independent measurement. ANOVA test revealed that the effect of density on the permeability is significant for strand alignment direction (p<0.001). Tukey's HSD test indicated that the permeability difference between any two density levels was significant

in each direction except for 625kg/m^3 and 700kg/m^3 for the 45° alignment. The variance for the 45° direction is higher than the measurements in the other two directions, especially at the high density range. The complete details of the ANOVA results are listed in Appendix B.

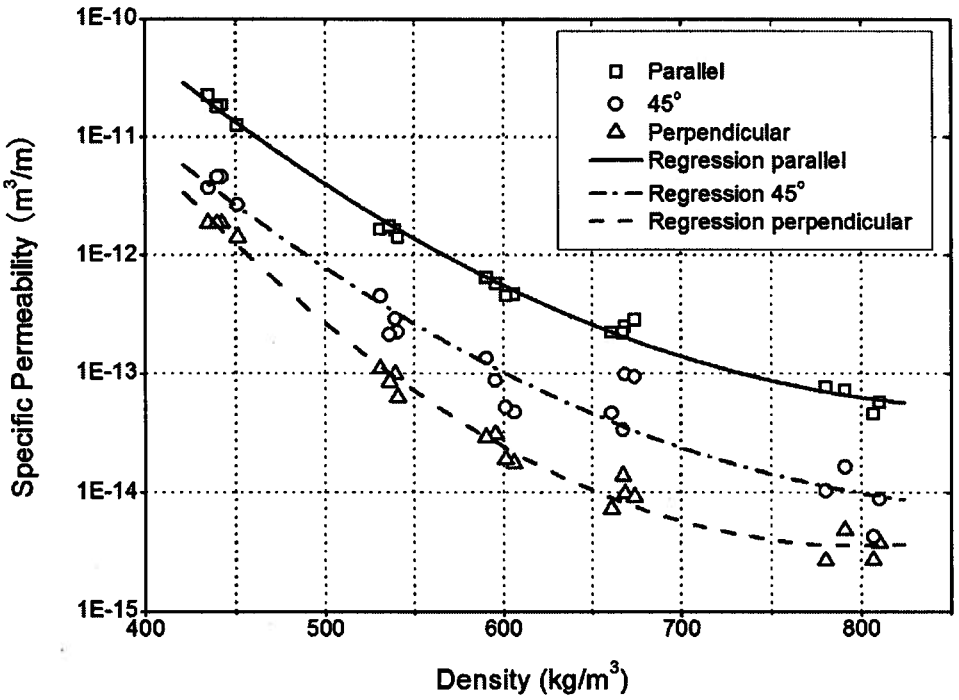

Figure 4.3: Permeability values and polynomial regression lines in different directions.

Permeability decreases as the density increases in all the three directions. The compaction of higher density panels causes more strand contact reducing the average volume and number of voids and their connectivity. Simultaneously the voids inside the strands are also compressed to smaller sizes. The flow paths can be divided into two types: inter-strand referring to the voids existing between strands, and intra-strand referring to those existing insides strands. In low density samples the flow through inter-strand voids dominates gas transportation. When the densification increases the inter-strand voids are compacted and closed causing the fluid to be forced through the intra-strand voids.

Comparing different air flow directions for a specific density, gas flows much more easily in the parallel direction, in Figure 4.3. Vessels in aspen provide long channels for gas passing through without much obstruction. However, if gas is forced in perpendicular

to strand direction, there are numerous layers of cell walls blocking in the way. For the air flow in 45° to strand orientation, gases can flow through the strands in a tortuous combination of these two directions; it lies between the parallel and perpendicular measurements and there is higher variation in the data.

This ratio of perpendicular and parallel permeability gives a measure of the anisotropy of the board. Figure 4.5 shows that the ratio K_{90}/K_0 is lower than 0.12 over the whole density range tested. It decreased with density below 700kg/m^3, after which increased slightly. The ratio of K_{45}/K_0 was more variable and there is a very slight downward trend with increasing density, but it is not significantly for the number of samples tested. It is found that the permeability parallel to the strands is 10-30 times greater than the permeability in the perpendicular direction.

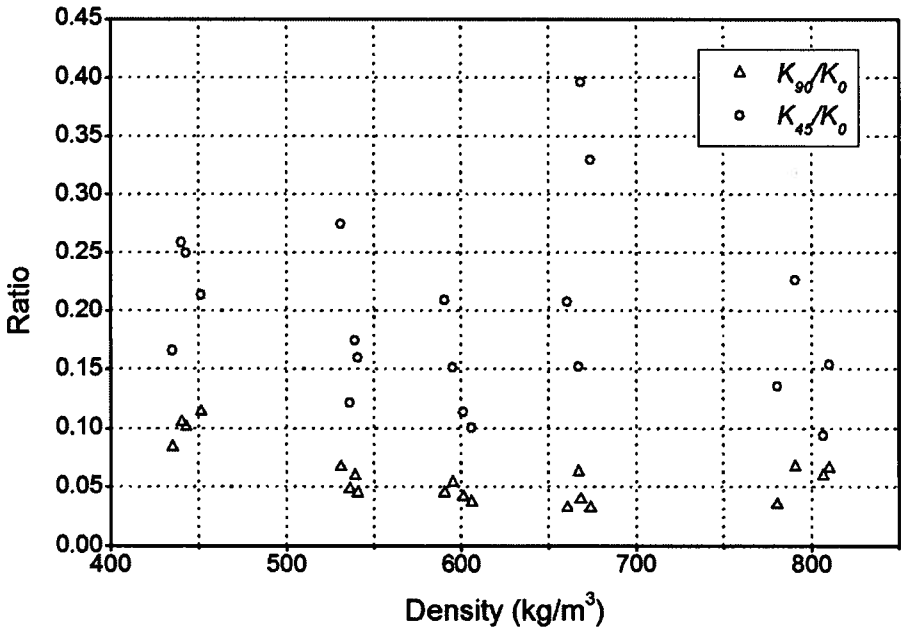

Figure 4.4: Ratio of permeability values in different directions representing the permeability anisotropy of the panels.

4.4 Regression analysis

When a linear regression was performed in each direction, it provided an unequal variance. Therefore, a second order polynomial regression was conducted to arrive at the empirical equations. The equations for the different directions are:

$$\lg(K_0) = -3.285 - 0.02261 \times \rho + 1.277 \times 10^{-5} \times \rho^2 \quad (r^2 = 0.993) \qquad (4.1)$$

$$\lg(K_{45}) = -3.944 - 0.02258 \times \rho + 1.250 \times 10^{-5} \times \rho^2 \quad (r^2 = 0.938) \qquad (4.2)$$

$$\lg(K_{90}) = -1.122 - 0.03333 \times \rho + 2.084 \times 10^{-5} \times \rho^2 \quad (r^2 = 0.988) \qquad (4.3)$$

where, K_0, K_{90}, and K_{45} are specific permeability, the subscripts indicate the angle between flow direction and strand orientation (m^3 /m); ρ is the oven-dried panel density (kg/m^3).

The goodness of fit of the polynomial regressions to the data is shown in Figure 4.3. As one can see the figure, the equations provide a good description of the permeability behavior in each direction.

4.5 Comparison with previous research

The in-plane permeability measurement of commercial LSL panels with two densities is shown in Appendix A. Figure 4.5 compares the results in parallel direction from laboratory-made thick, oriented strand-based panels and commercial LSL panels. LSL panels have slightly higher permeability than lab-made panels at the same density. The reasons for the differences included the difference in strand sizes, resin content, press cycles, strand forming technique, and raw materials. One of the key factors may be the forming of strands. The panels manufactured in the lab optimized strand orientation and mass distribution by hand forming, which could not be as well achieved in industrial process. For the same density LSL panel has more visible voids also with larger sizes leading to a higher permeability. Another factor could be the shape of strands: LSL strands used here are longer with a smaller width/thickness ratio creating more voids which are also more interconnected.

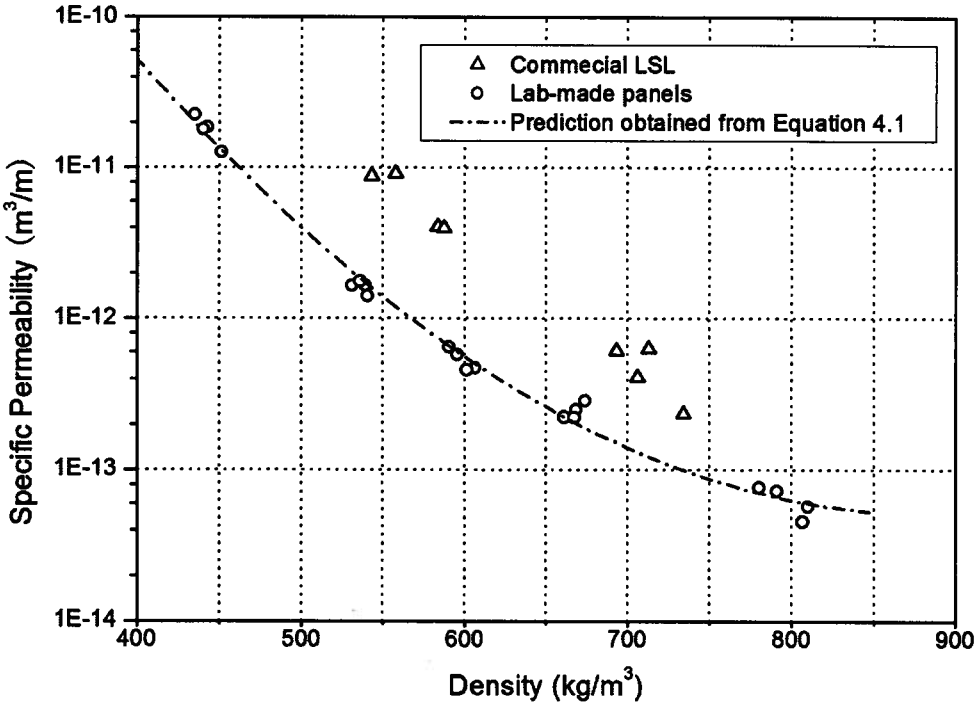

Figure 4.5: Comparison between laboratory-made panels and commercial LSL in parallel direction.

A study on in-plane permeability of unresinated OSB mats was presented by Hood (2004) and Hood *et al.* (2005). The strands used were yellow-poplar (*Liriodendron tulipifera*); they were about 100.0 mm (4.0") long, 25.4 mm (1.0") wide and 1mm thick; no adhesive was used in the formation of mats with the exception of 800 kg/m^3 ones (3% PF resin). Hood *et al.* (2005) provided Equation 2.14 and 2.15 to predict the in-plane superficial permeability for air. The input variables were compaction ratio C and strand thickness t. According to the property of aspen strands (oven-dried density 403.87 kg/m^3), the compaction ratio C is calculated as $C = \rho/403.87$, t = 1 mm, and $\eta = 1.846\times10^{-5}$ Pa·sec (air at 25°C) to compute the specific permeability.

The comparison between the prediction according to Hood *et al.* (2005) and that obtained from Equation 4.1 (regression obtained from this research) is shown in Figure 4.6.

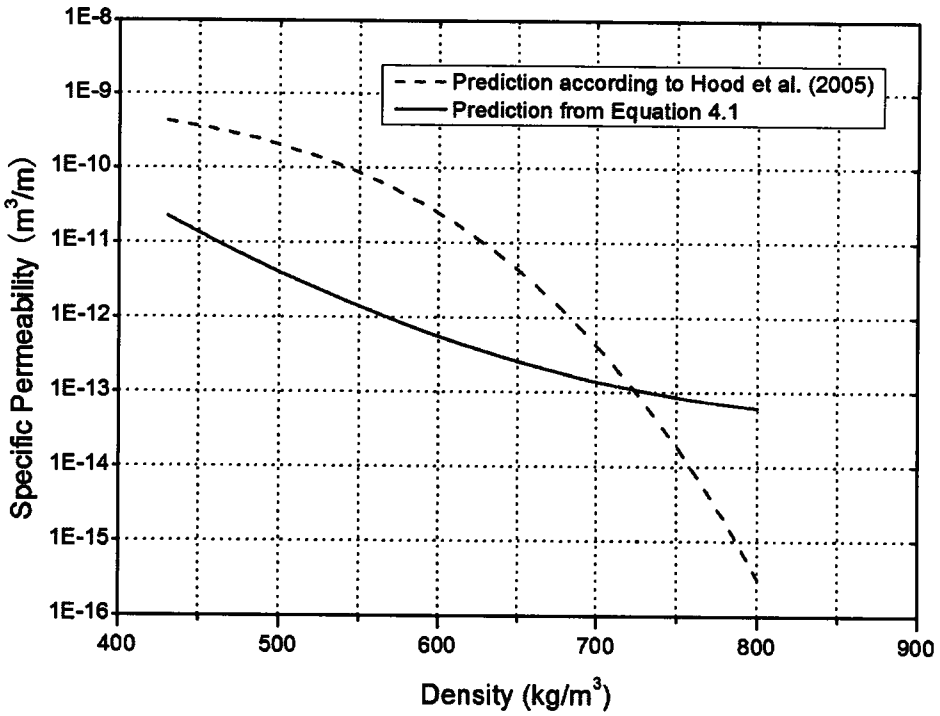

Figure 4.6: Parallel permeability prediction based on Hood et al. (2005) compared with the prediction from Equation 4.1.

The prediction from these equations differs remarkably. In both cases the permeability decreases with increasing density, but for Hood's prediction, the rate of decrease accelerates whereas the Equation 4.1 decelerates with the two curves intersecting at about 720 kg/m^3. The reasons creating the difference between the two predictions include the wood species, resin content, pressing process, and strand sizes. Because of lacking information, it is difficult to determine which of them plays a more important role.

The ratio of perpendicular to parallel permeability is compared in Figure 4.7. The ratio for Hood's work was much higher and increased with density indicating that the panels made by Hood *et al.* (2005) were less anisotropic. It could have been caused by the strands not being well oriented.

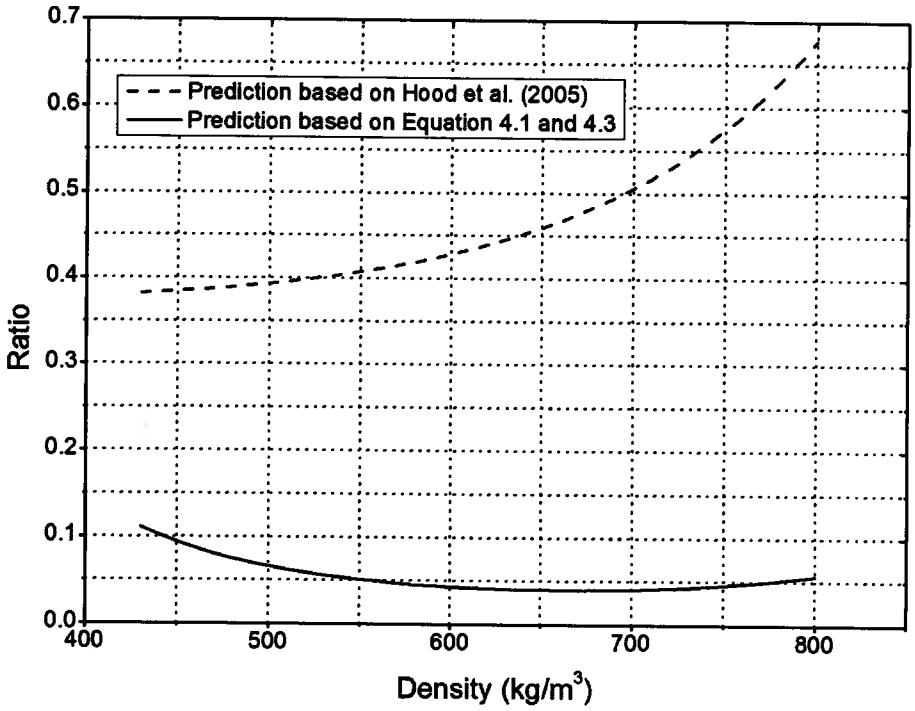

Figure 4.7: Compare the ratio of perpendicular and parallel permeability with Hood et al. (2005).

Haas *et al.* (1998) measured the in-plane permeability of OSB panels in both parallel and perpendicular to strand orientation directions. For a resin content of 5%, they fit the results to the following equation:

$$K_{parallel} = \exp\left(\frac{1}{-0.049 - 3.22\times10^{-6}\times\rho - 0.540\times\rho}\right) \qquad (4.4)$$

The prediction of Haas *et al.* (1998) is compared with that given by Equation 4.1 in Figure 4.8. The two curves have similar trending and both the slopes are decreasing with density. Although Haas *et al.* (1998) yields a slightly higher estimate, the predictions are all in the same order of magnitude. The difference could have been caused by two reasons: the strands used for this work were thicker, and more oriented providing less void space and reduced its connectivity.

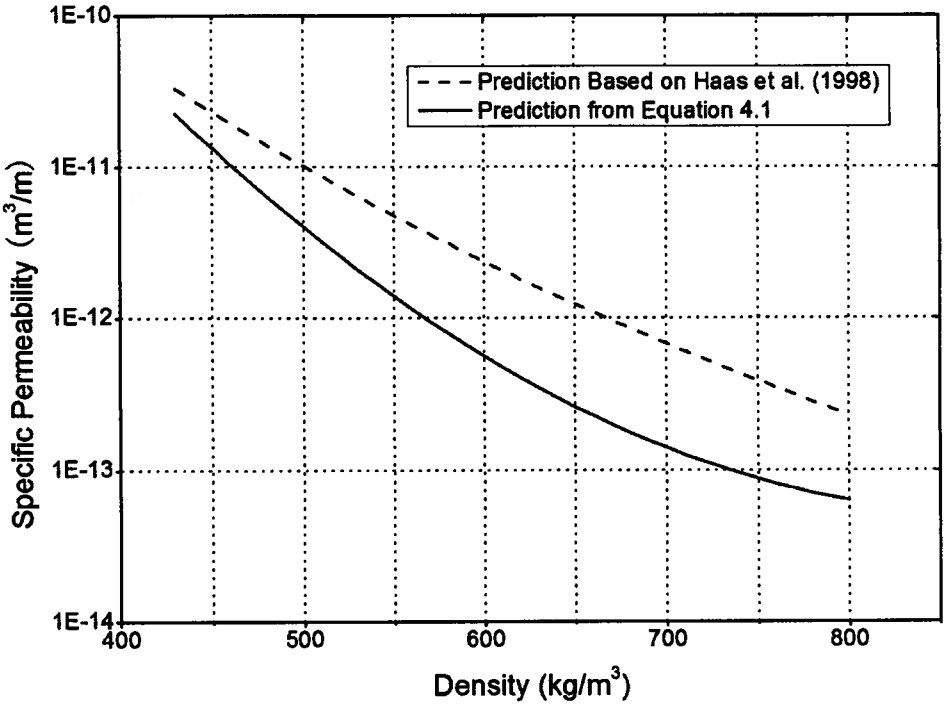

Figure 4.8: Parallel permeability prediction from Haas et al. (1998) and prediction from Equation 4.1.

5 Microscopic Investigation on Void Structures

The voids in strand-based wood composites can be categorized as inter-strand or intra-strand depending on their locations. The densification that occurs during hot-pressing permanently changes the size and connectivity of these voids and yield different product properties. This chapter investigates the effects of densification on void structures by revealing the shape and state of voids in the finished panels pressed to different densities using optical microscopy.

5.1 Material and methods

One could section the OSL samples in any number of ways to examine the void microstructure, but the this work focuses on sections whose plane is perpendicular to the strand alignment direction as shown schematically in Figure 5.1. At first the samples were cut into 10 mm by 10 mm by 20 mm and sliced by a sledge microtome equipped with FEATHER S35 stainless steel blades. The thin sections produced were found to be brittle, cracked, and broken easily so that the voids may not correspond to the true state of voids in the original sample. To improve their integrity the samples were vacuum impregnated with a low viscosity epoxy-based thermosetting resin (Industrial formulators Cold Cure epoxy), epoxy left to cure for 12 hours, and sections microtomed as before. However, the epoxy impregnated samples became too hard and dulled the microtome blades quickly resulting in a surface with substantially damage.

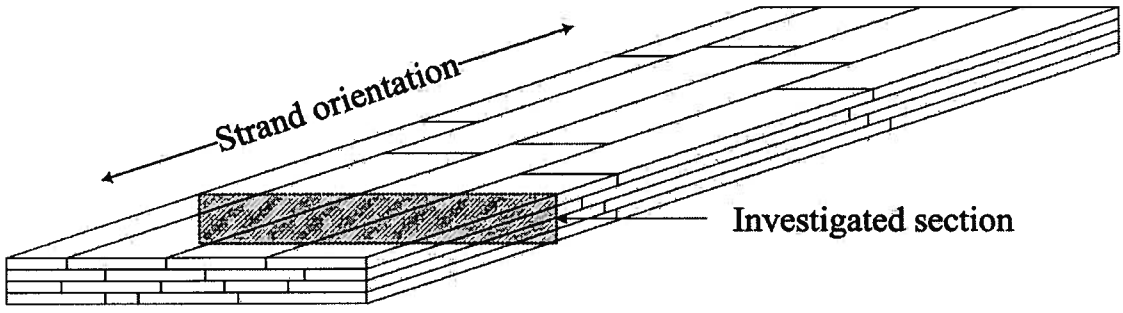

Figure 5.1: The location of an investigated section in a panel.

Another method, which has been commonly used in petrographic examination of construction materials, e.g., rock, cement, and concrete, was used to prepare samples. The

procedure can be briefly stated as: a thick sample section is cut, bonded to a microscope glass slide, and then sanded to the required thickness and surface smoothness.

Epoxy was initially used to bond the sample section and glass slide together. The images obtained indicated that a significant amount of epoxy penetrating into the cell structures had covered and prevented a clear view of void structures as a result of the small molecular size of epoxy components. As shown in Figure 5.2, the black areas are cell lumens, while the white areas are filled with epoxy resin. To remove the epoxy, part of the slide was immersed into a methylene chloride based solvent, paint stripper. After three hours, the epoxy had completely dissolved, but the section itself had also swelled and separated from the glass slide. At this point it was concluded the application of epoxy was not workable.

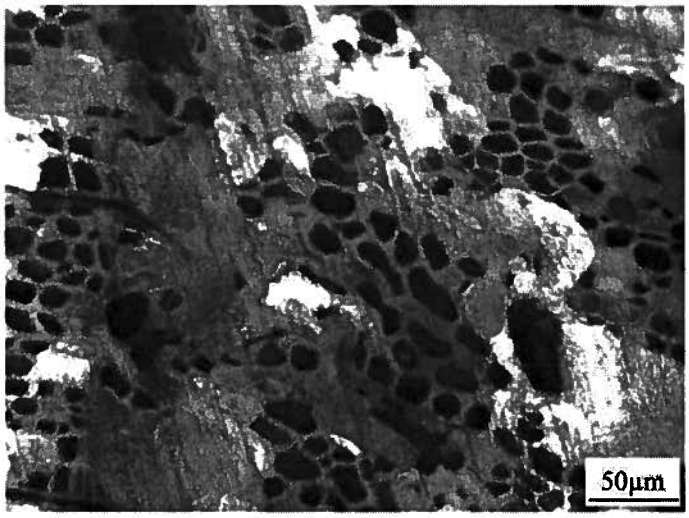

Figure 5.2: Epoxy impregnated sample sections. The white areas are filled with epoxy.

The next approach tried was to use hot melt adhesive (Scotch-Weld™ 3738AE) to glue the section to the microscopy sides. This technique was successful by eliminating the penetration of the glue and yielding clear images. The detailed procedure is listed here:

1. Four specimens were randomly selected from each density level, and a slide prepared for each specimen. The samples, 50.8 mm long and 25.4 mm wide, were cut from the boards (thickness 31.8 mm) and oven dried until a constant weight was achieved.

2. A surface was prepared for sanding with a series of finer and finer sand papers 80, 120, 180, 220, 330, 400, 800, and finally 4000 grit. When the dust accumulated it was blown away by high pressure air (about 250 kPa). The purpose of this stage is to ensure clean surface for bonding the glass slide.

3. The prepared surface was bonded to a glass microscopy slide with hot melt adhesive. To achieve a thin, relatively uniform layer of hot melt adhesive on the slide, it was heat to about 70°C on a hot plate. The section was pressed down to the molten adhesive, removed from the hot plate and allowed to cool.

4. After the adhesive cured the glass slide and a thick sample section (about 3-4 mm) of the sample were carefully cut off with a hand saw, as shown in Figure 5.3b. A precision saw would be a better choice if available.

5. The thick section was sanded to less than 300 μm with abrasive papers of 80, 120 and 180 grit, and then polished with successively finer abrasive papers of 220, 330, 400, 800, and 4000 grit until a high quality damage free surface was obtained. Similar to step 2, the dust was blown away with high pressure air to prevent coarser dust remaining on the surface. The finished slides are shown in Figure 5.3c.

Figure 5.3: Slide preparation processes: (a) samples bonded to glass slide, (b) thick sections cut off with slides, (c) finished slides after sanding.

This method is a dry process requiring no solvent and maintains the original structure of voids. The downside of this technique is that it is time-consuming and requires about 3 hours to finish one slide. The efficiency can be improved with the help of grinding/polishing machines if necessary. Jana (2006) suggested three types of common grinding machines and Buehler™ supplies an assortment of equipment for sectioning,

bonding, grinding, and polishing for petrography, but such equipment was not available for this work.

After the slides were prepared, they were examined using a JENAMED 2 light microscope, a picture of which is shown in Figure 5.4. A Lumenera Infinity 3 camera was connected to the microscope to capture and record the images. All the microscopic images in this chapter, e.g., Figure 5.5, are shown with the width of each section horizontally corresponding with thickness of the original panels.

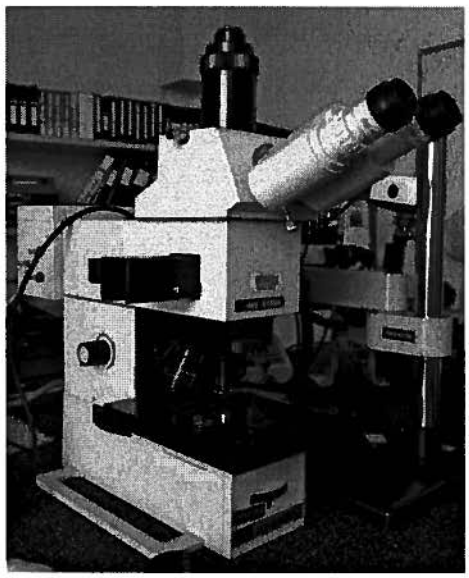

Figure 5.4: JENAMED 2 light microscope for slide investigation.

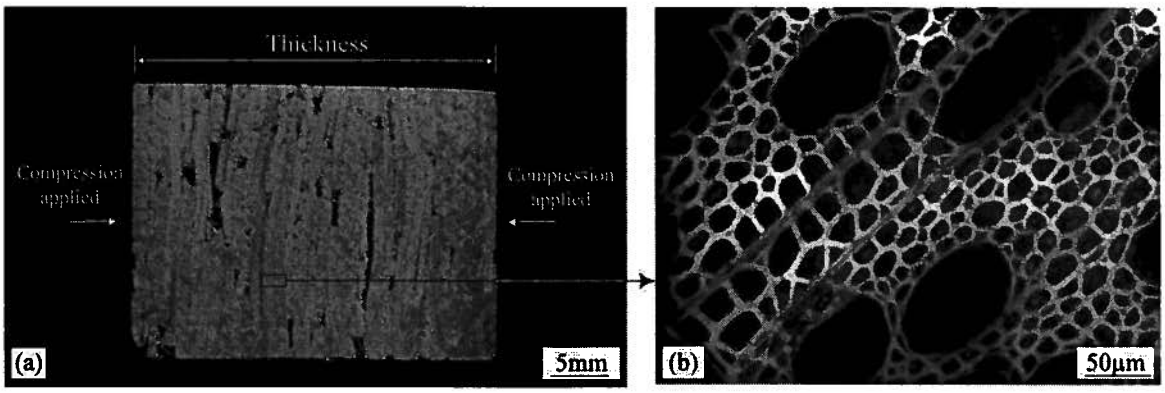

Figure 5.5: Image orientation on a cross section: (a) location of the image on a cross section, (b) image obtained from microscope (450kg/m^3).

5.2 Results and discussions

5.2.1 Inter-strand voids

Intuitively, one would expect that increasing densification creates more contact area between strands and decreases the voids volume between them. Comparing the thickness morphologies of panels pressed to different densities, Figure 5.6 shows that this is indeed the case. Many voids are visible for the 450 kg/m^3 sample, Figure 5.6a, the two largest of which are circled; fewer voids and smaller voids for the 550 kg/m^3 sample, Figure 5.6b, and fewer voids still for the 625 kg/m^3, Figure 5.6c, the two largest of which are also substantially smaller than those for the 550 kg/m^3 sample. For the higher density samples, Figures 5.6d and e, no voids are seen indicating that the density at which the maximum contact area between the strands is reached between 625 and 700 kg/m^3.

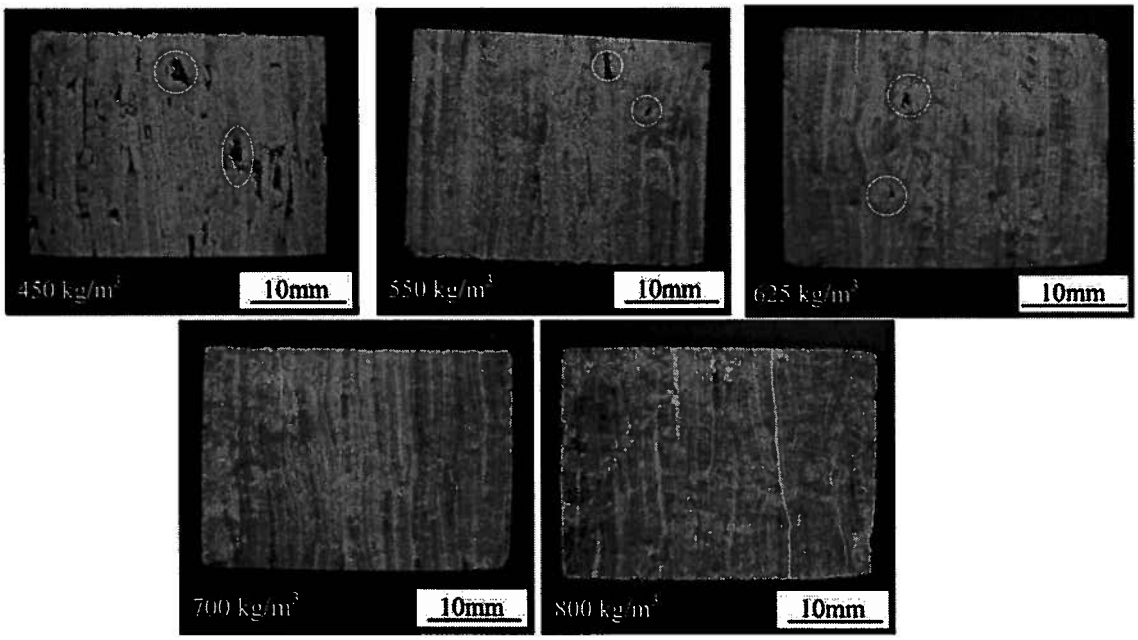

Figure 5.6: Comparison of the number and size of inter-strand voids for typical sample sections of each panel density (cross-sections perpendicular to strand orientation, some voids are circled to highlight).

Close examination of the lowest density section in Figure 5.6a at a higher magnification, as shown in Figure 5.7, suggests how voids are formed during densification. As shown in Figures 5.7a, and 5.7b, when strand layers overlap each other, the adjacent strands create

bridges at the end of one or more strands and form inter-strand voids of rectangular or triangular shape. The longer and wider voids are eliminated by compression first because the strands over these voids tend to have larger displacements when applying the same compression forces, as shown in Figure 5.8a and 5.8b. It has also been supported by the images obtained for high density samples (Figure 5.6), in which voids have a lower length/width ratio.

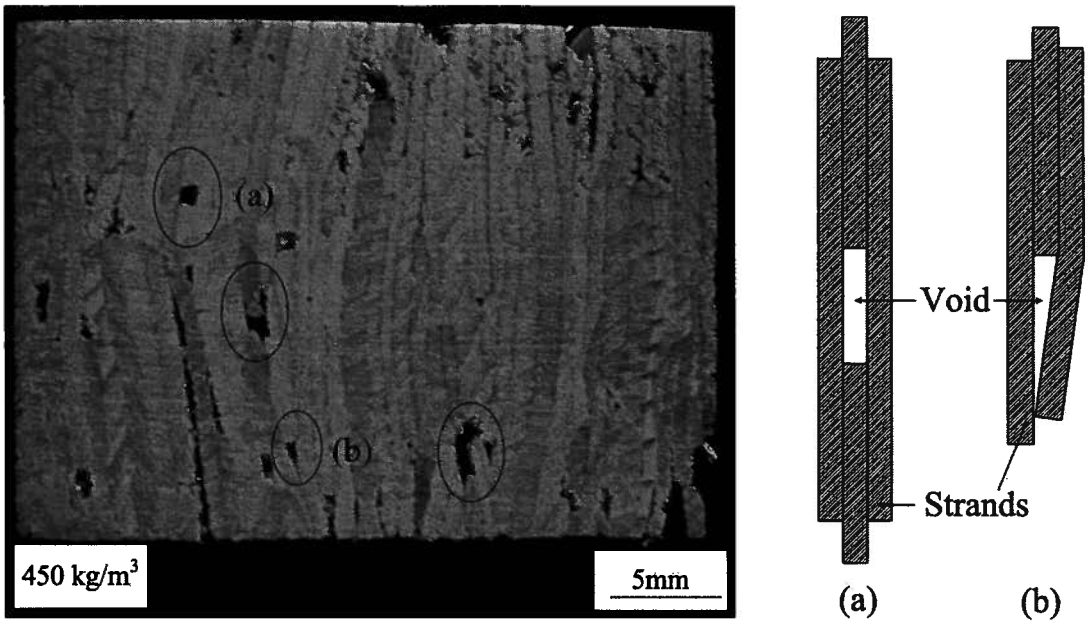

Figure 5.7: The formation of inter-strand voids: (a) rectangular shaped void, (b) triangular shaped void.

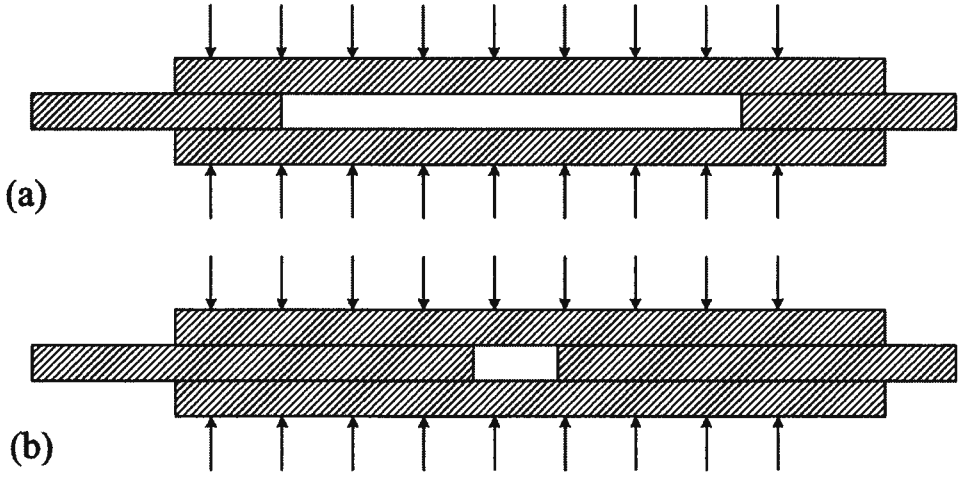

Figure 5.8: Comparison of long and short voids in compression: (a) long void, (b) short void.

Observing under microscope with a magnification of ×25, the areas between strands presented two types of phenomena: voids as brighter areas and strand contacts at strand boundaries (Figure 5.9).

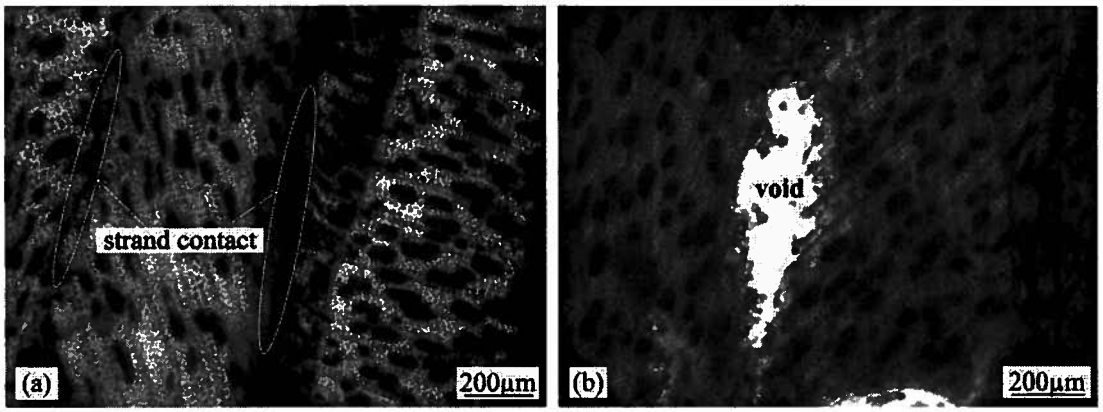

Figure 5.9: Thin sections of 625kg/m^3 samples viewed under transmitted light microscope showing: (a) interfacial contact areas between adjacent strands and (b) an inter-strand void region that has been impregnated with hot melt glue.

The voids appeared here brighter than other part was because of the penetration of hot-melt which easily transmits light through the slide. 450kg/m^3 samples revealed long and continuous voids, while 550kg/m^3 and 625kg/m^3 samples showed less inter-strand voids. For 700kg/m^3 and 800kg/m^3 samples only one or two inter-strand voids were found on a full-thickness slide. From the macroscopic and microscopic investigations, it could be concluded that the inter-strand voids decreased in size and quantity with increasing panel densification.

Figure 5.10 shows the contacts between strands. The areas close to strand boundaries are more compressed than those some distance away. The voids created by strand contact were smaller than the cell lumens in the strands.

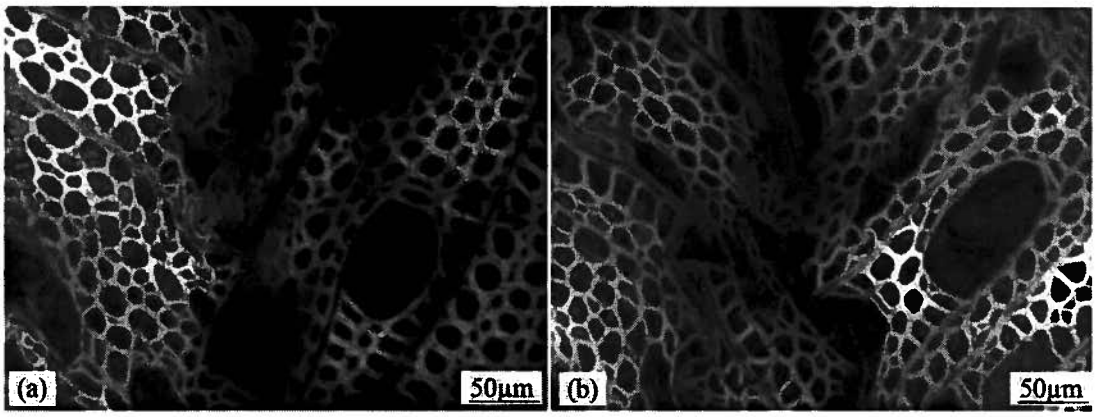

Figure 5.10: The contact points between two adjacent strands: (a) the area close to strand edge is more compressed, (b) inter-strand void is smaller than intra-strand voids.

5.2.2 Cell structure compression

The increasing densification also significantly changes cell structures of the strands. The various different stages of cell deformation are described in the following enumerated list. Note that due to the large variability possible plane of strand surfaces, i.e., longitudinal-radial, longitudinal-tangential, or anything in between these extremes and not to mention the additional complexity that is created in describing the wood plane should the log being stranded not be correctly oriented in the strander, the following list of cell deformation stages shown in Figure 5.11 is qualitative only:

a. Non-compressed stage when the vessels and fibers remain their original state. The vessels are circular or sub-circular shaped.

b. Vessel initial deformation stage when the circular vessels start to deform to an oval shape. The deformation of fibers is not significant enough to be observed.

c. Vessel secondary deformation stage. Vessels deform to an extent that their curvature edges have become straight. Fiber deformations are also observed now. During stages a, b, and c, the rays remain their original orientations without any deformation happened.

d. Ray initial deformation stage. The significant change is that the rays start deforming from straight lines to curves. And the cell arrays between them are distorted.

e. Ray secondary deformation stage. The vessels are compressed to a shape of high length/width ratio. The width of vessels is still two or three times that of the adjacent fibers. The fibers have also further deformed to irregular shapes and those at the same columns with vessels deform much more than others.

f. Width uniform stage. The vessel width has been pressed to the same size as the fiber width.

g. Final densification stage. Both vessel and fibers are substantially compressed and much distorted from their original shapes. Their sizes become almost the same in length and width. The lumen closing up of some vessels is also observed.

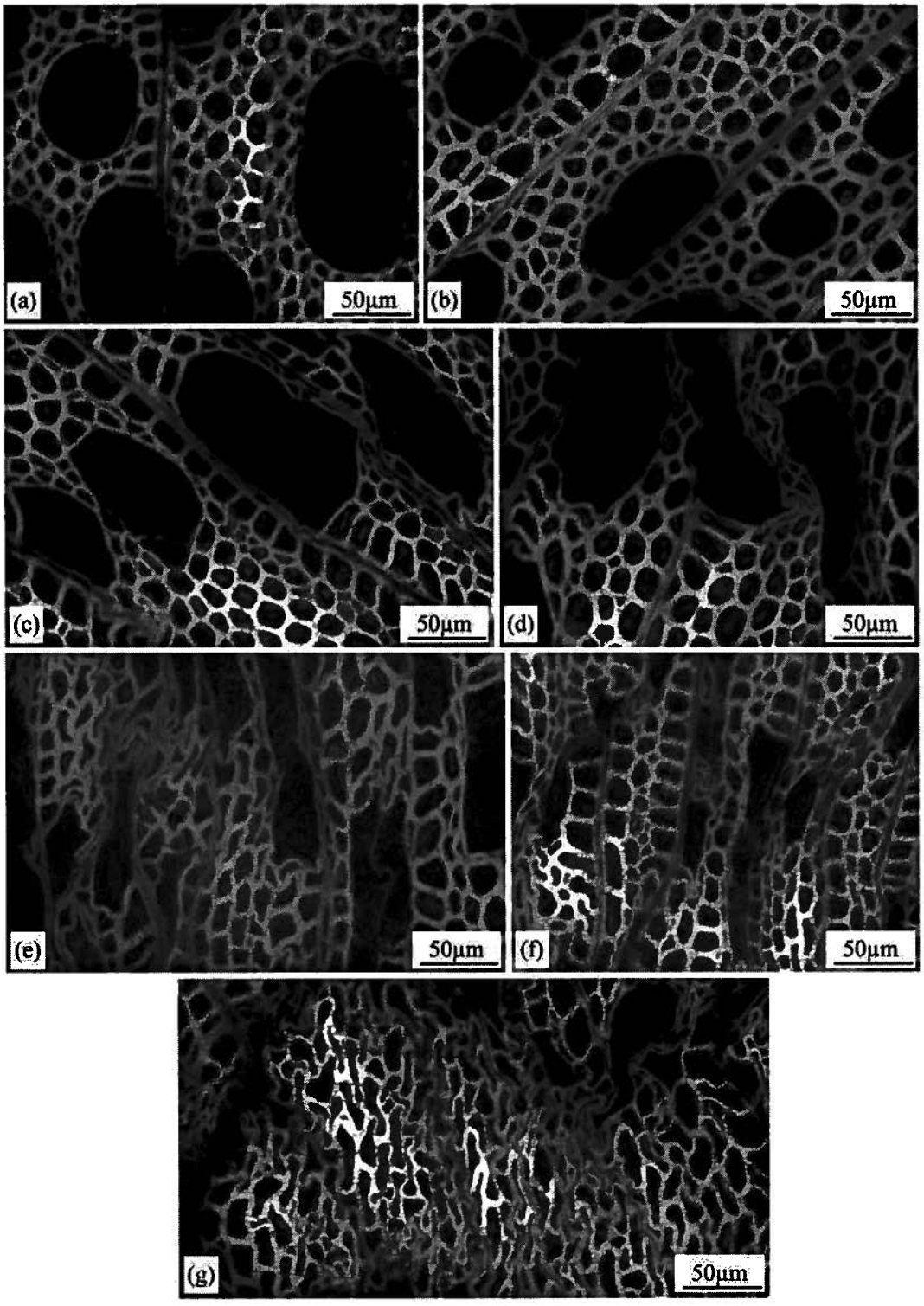

Figure 5.11: Cell structure compression stages: (a) non-compressed stage, (b) vessel initial deformation stage, (c) vessel secondary deformation stage, (d) ray initial deformation stage, (e) ray secondary deformation stage, (f) width uniform stage, (g) final densification stage.

The damage of cell walls always accompanies the deformation of a vessel or a fiber. The main failure of cell walls is caused by buckling under an axial load, as shown in Figure 5.12a. When the cell wall is not parallel to the load direction in certain areas, it collapse in a more complex way under both axial and lateral loads, as shown in Figure 5.12b. The failure of cell walls decreases the original cell wall length and the size of cell lumens drastically and plays an important role in the changing of intra-strand void structures.

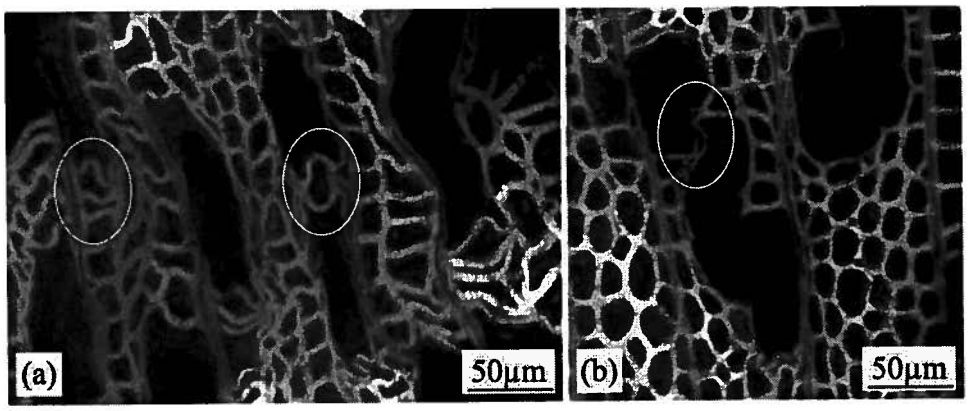

Figure 5.12: Cell wall failures (circled): (a) buckling under axial loads, (b) failure under both axial and lateral loads.

5.2.3 Variability of intra-strand void deformation

The voids existing inside a strand refer to fibers and vessels in aspen. The eight stages introduced above cover a general process of a strand compressed from beginning to the end. However, for a combination of strands different compression stages coexist. As shown in Figure 5.13, both non-compressed strands (Figure 5.13a) and compressed strands (Figure 5.13b) are present in a 450 kg/m^3 sample. Figure 5.14 shows the distinctly different compression stages are found in 800 kg/m^3 samples.

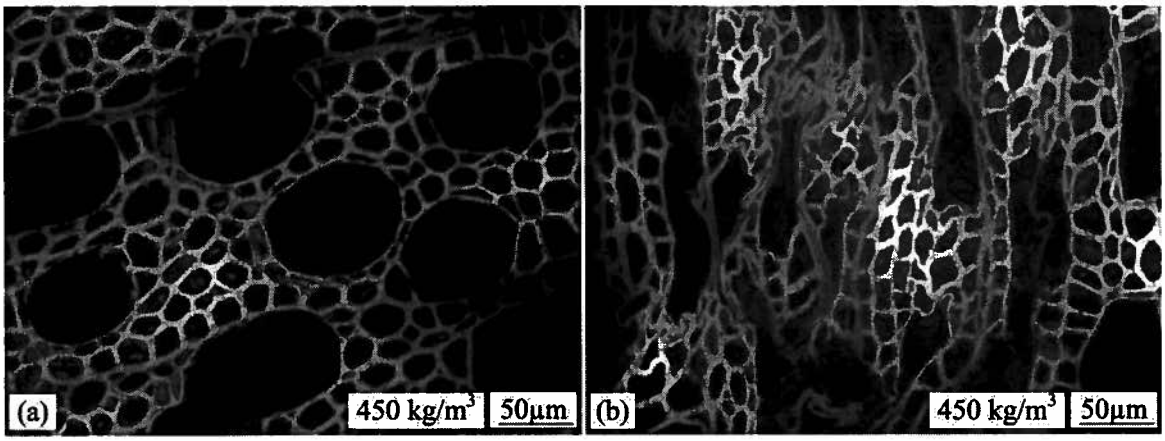

Figure 5.13: Different compression stages coexisting in 450 kg/m^3 samples: (a) cells at non-compressed stage, (b) compressed cells at ray secondary deformation stage.

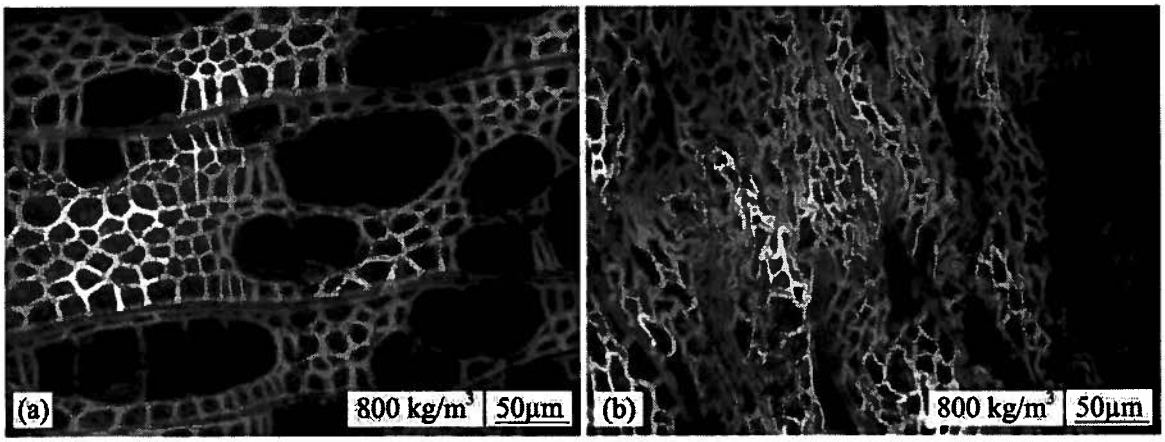

Figure 5.14: Different compression stages coexisting in 800 kg/m^3 samples: (a) compressed cells at vessel initial deformation stage, (b) compressed cells at final densification stage. .

Difference not only occurs between strands in one sample, but also inside one specific strand. The vessels in aspen, surrounded by thin-walled paratracheal parenchyma, are of larger diameters than fibers. They are also conductive elements with numerous pits causing them to be weaker than thick-walled fibers (Tabarsa and Chui 2001, Panshin and deZeeuw 1980). Therefore, the vessels should be easier to compress than fibers, and the microscopic observation in Figure 5.15 supports this conclusion.

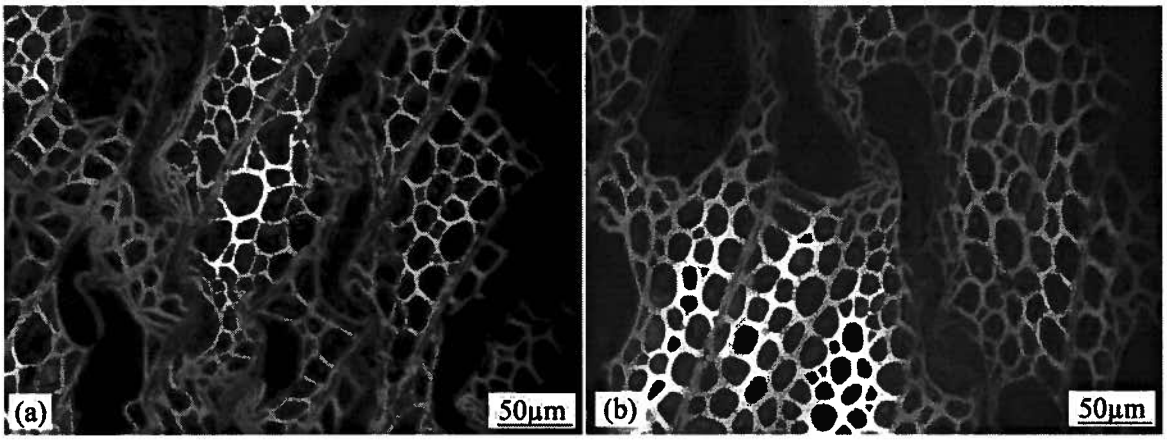

Figure 5.15: Different compression behaviors of vessels and fibers.

In addition to that, sometimes the entire row of cells fails first, shown in Figure 5.16a. A few weaker vessels also collapse ahead of other ones, shown in Figure 5.16b.

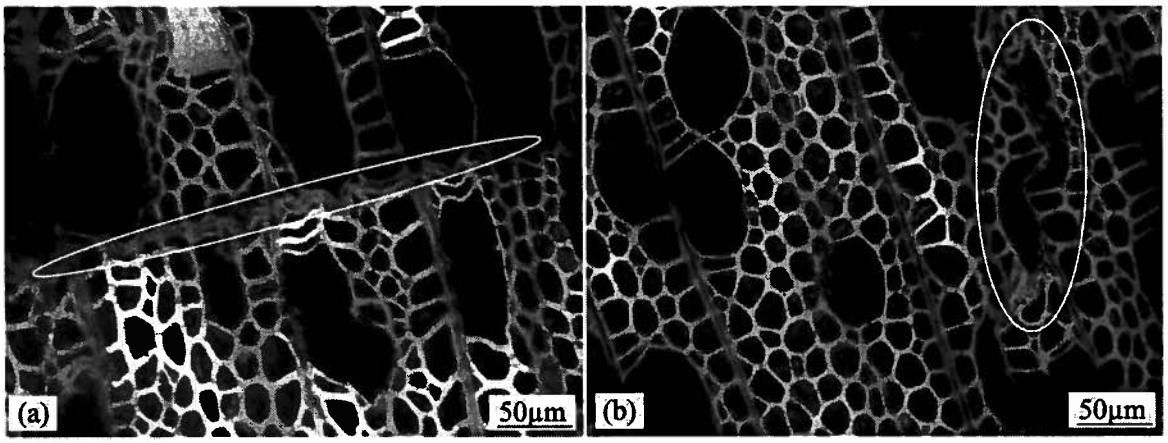

Figure 5.16: Non-uniform compression inside one strand: (a) one entire row fails first, (b) some weaker vessels collapse ahead of others.

The variability of strand structures could be caused by the following reasons:

1. Strand lay-up: as a result of the strand size difference, the strand lay-up process will produce a three-dimensional density variation inside a panel, where the high density area tends to be more compressed.
2. Strand cutting orientation: the strand length is along the longitudinal direction of a wood, while the cross-section could be cut from a tangential orientation or a radial orientation. As shown in Figure 5.17, A, B, and C illustrate three different cutting

orientations and ray patterns, and Figure 5.18 shows the microscopic level of the strands. Generally when applying compression perpendicular to the strand surface, strand A has higher elastic modulus, second is strand C, and strand B has the lowest (Wood Handbook, 1999).

3. Growing and treatment conditions: the growing environment, local climate, treatment conditions after logging, and the location of a strand in a log all create variabilities in strand properties, especially the elastic modulus, which yield different behaviors of strands under compression.

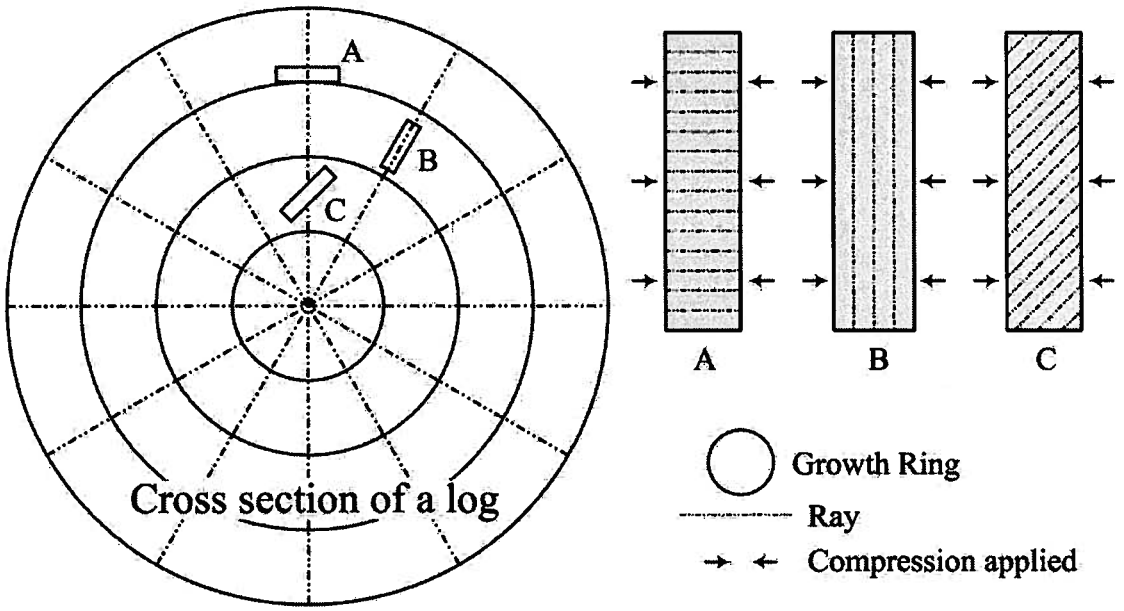

Figure 5.17: Variation in strand cutting orientation: Strand A was cut from longitudinal-tangential (LT) direction; Strand B was cut from longitudinal-radial (LR) direction; Strand C was cut from a direction between LT and LR. The lines in the strands indicate the direction of rays.

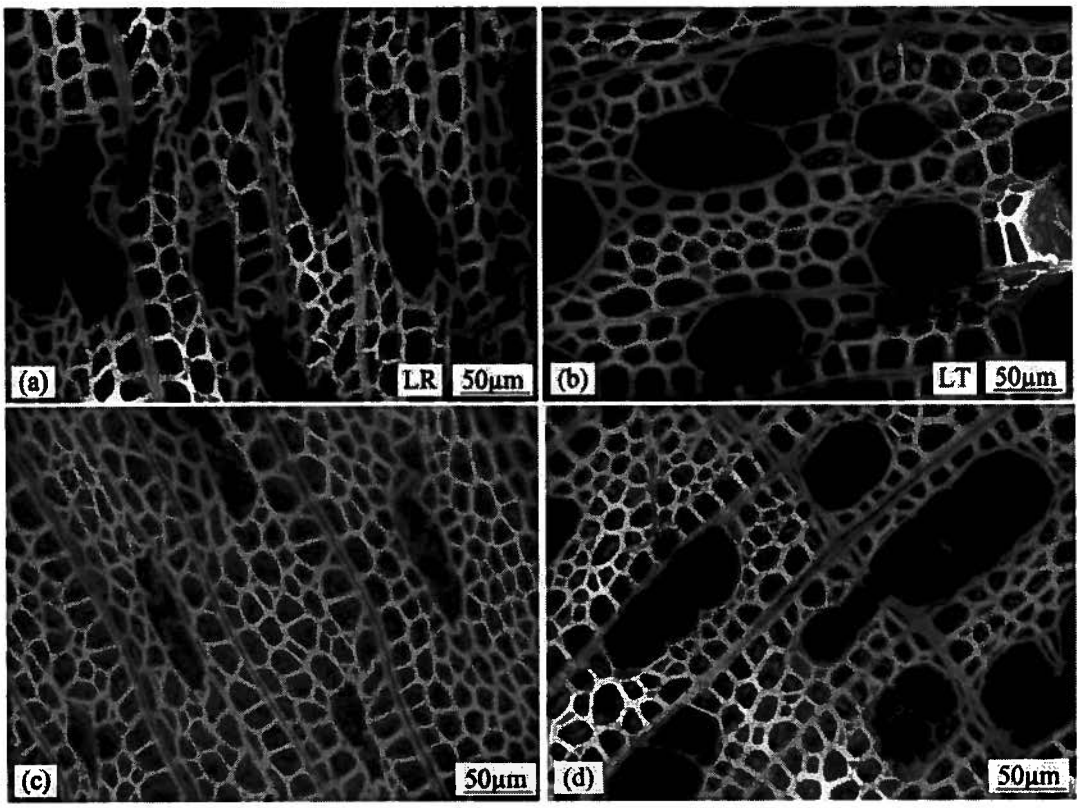

Figure 5.18: Strand cut from different orientations: (a) strands cut in LR direction, (b) strands cut in LT direction, (c) and (d) strands cut in a direction between LR and LT.

When comparing panels with two densities, e.g., 400 and 800 kg/m^3, the former has more strands staying at non-compressed stage to ray initial deformation stage, while the latter has more at ray secondary deformation stage to final densification stage. However, it is difficult to quantify the proportion of each compression stages in a sample with the results obtained currently.

5.2.4 Other features

As introduced in Section 5.2.3, vessels are easier to be compressed and deform more than fibers. However, a few strands behave in an opposite way, as shown in Figure 5.19. The fibers between vessels are severely compressed while the vessels still have a large lumen area.

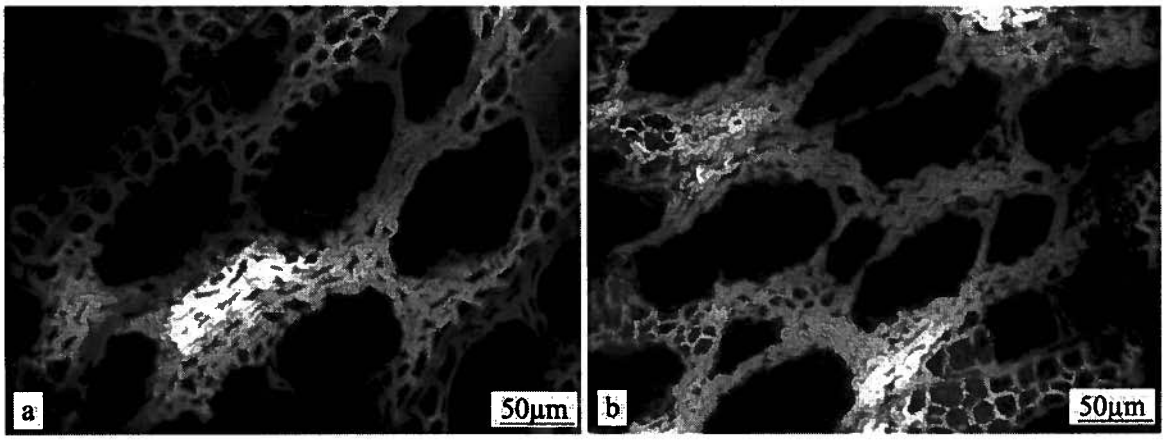

Figure 5.19: Special vessel-fiber compression pattern.

One or two pieces of softwood strands were found in the samples, as shown in Figure 5.20a. The pattern of cell wall failures in softwood is different from that found in hardwood. In aspen the vessels and fibers deform non-uniformly as a result of their difference in diameter and cell wall thicknesses. Figure 5.20b indicates that the entire rows of tracheids failed simultaneously, as result that has also been found by Bodig (1965) and Geimen *et al.* (1985).

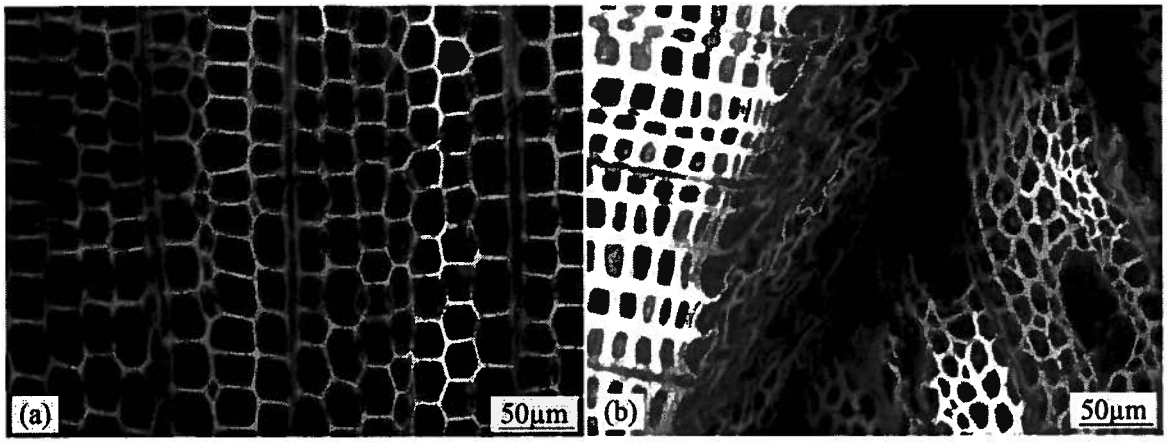

Figure 5.20: Existence of softwood strands: (a) uncompressed softwood cells, (b) entire row of tracheids failed when compressed.

5.2.5 Summary

The investigation of void structures in finished panels pressed to different densities found the development of inter-strand and intra-strand void as densification increases. A high

variation of compression occurred within one strand as well as within one specimen. A series of compression stages was used to generalize the cell structure changes with compression. With the results a mathematical model will be developed in Chapter 6 to quantify the void geometry of oriented strand-based panels, which will be related to the flow transportation afterwards.

6 Permeability Modeling

6.1 Basic concept

Gas flow through strand-based wood composites is a complex phenomenon determined by many different parameters, for example: (i) the flow regime is laminar or turbulent; (ii) the flow is steady-state or transient; (iii) the flow is one, two, or three dimensional; (iv) the fluid is Newtonian or non-Newtonian; (v) the field is isothermal or temperature dependent; (vi) the flow is single phase or multi-phase; (vii) the fluid is incompressible or compressible (Kleinstreuer 1997). The liquid is usually assumed to be an incompressible single phase Newtonian fluid with constant dynamic viscosity. Depending on the experimental conditions applied during this work, the flow can be laminar, steady-state, one-dimensional, and isothermal. The strands are assumed to be identical size and are uniformly compressed to yield an evenly distributed density in three dimensions.

As introduced in Chapter 5, the flow through strand-based wood composites can be categorized into two types according to the location: inter-strand and intra-strand. In the model of intra-strand flow, no inter-strand flow will be considered. The effect of inter-strand voids is then added to describe and predict the flow occurring in an oriented strand based wood composites. From the results in Chapter 5, the flow in the direction parallel to strand orientation is the controlling factor for the overall fluid transportation. Therefore, only the model of permeability in this direction is developed.

6.2 Modeling on intra-strand flow

Intra-strand flow refers to the fluid passing through the elements within a strand, i.e., fibers and vessels. For aspen (*Populus tremuloides*) vessels and fibers have an average length of 670μm and 1320μm respectively; the frequency of vessels per unit volume was in the range of 85-180 per square millimeter with the diameter ranging from 50-100μm (Panshin and Zeeuw 1970).

Flow through these elements is also dependent on their connectivity. Two consecutive vessel elements are connected by a perforation plate: aspen has simple perforation plates,

where a single opening occupies almost the entire plate (Hoadley 1990). Therefore, an aspen vessel can be simplified as a pipe with a constant cross section. The structure of fibers is quite different from vessels: they have closed ends and flow through them is much more difficult than for vessels (Panshin and Zeeuw 1970). In this model, the fibers are assumed to be impermeable.

The longitudinal flow in aspen can be simplified as occurring in thousands of micro-pipes with impermeable walls because the longitudinal permeability is much higher than the transverse permeability (Siau 1995) and the vessel element is open throughout the sample. The basic concept of modeling intra-strand flow is that flow occurs only in aspen vessel elements, which can be considered as micro-pipes of constant diameter. The average diameter, quantity, and flow rate in one unit pipe will be determined, and then the sum of flow in all the pipes will be the flow of the whole sample.

For oriented strand based wood composites, the length of these pipes is limited to the length of a strand. Therefore, the flow through strand boundaries will be investigated.

6.2.1 Modeling based on rectangular void shapes

Sutton and Tardif (2005), and Kostiainen *et al.* (2008) measured the microscopic geometry parameters of aspen (*populous tremuloides)*, listed in Table 6.1.

Table 6.1: Microscopic geometry parameters of aspen measured by two different authors (standard deviation in brackets).

Parameters	Kostiainen *et al.* (2008)	Sutton and Tardif (2005)
Vessel lumen area fraction (%)	29.6 (5.6)	32.42 (4.24)
Vessel lumen diameter (μm)	51.5 (9.3)	48.6 (5.1)
Cell wall area fraction (%)	44.5 (4.6)	44.60 (2.88)
Fiber lumen diameter (μm)	10.6 (1.0)	17.2 (1.6)

The original vessel shape is circular or oval while when compressed it approaches to a rectangular shape (Figures 5.11 and 5.12), as found by the microscopic investigation in Chapter 5. The steady laminar full developed flow in a rectangular duct with constant cross section has the following velocity distributions (Rohsenow *et al.* 1998):

$$u = -\frac{16}{\pi^3}\left(\frac{dp}{dx}\right)\frac{a^2}{\eta}\sum_{n=1,3,\ldots}^{\infty}\frac{(-1)^{(n-1)/2}}{n^3}\left(1-\frac{\cosh(n\pi y/2a)}{\cosh(n\pi b/2a)}\right)\cos\left(\frac{n\pi z}{2a}\right) \qquad (6.1)$$
$$-a \le y \le a, -b \le z \le b$$

where η is the dynamic viscosity (Pa sec), a is half the thickness (mm), and b is half the width (mm) of the cross section.

Jong and Kwak (2008) presented the volumetric rate:

$$Q/t = -\frac{4ba^3}{3\eta}\left(\frac{dp}{dx}\right)\left(1-\frac{192a}{\pi^5 b}\sum_{n=1,3,\ldots}^{\infty}\frac{\tanh(n\pi b/(2a))}{n^5}\right) \qquad (6.2)$$

According to the measurement by Kostiainen *et al.* (2008), the vessels, with an average diameter of 51.5 μm, occupy 29.6% of the overall area and the incompressible cell walls fill another 44.5%. To keep a consistent calculation of rectangular lumen shapes, the original circular vessel is transferred to a square of the same area:

$$\pi D^2/4 = a^2 \quad \Rightarrow \quad a = w_0 = 45.64\mu m \qquad (6.3)$$

With the same method, a fiber lumen at the original state is also represented by a square of 9.39 μm.

Recall the compression stages defined in Chapter 5, vessels and fibers behavior differently during compression. There are two extreme conditions: type (a) - vessels and fibers deform simultaneously during the whole compression, shown in Figure 6.1a; type (c) - the other extreme is that only vessel elements contribute to the strand deformation while fibers keep their original sizes, shown in Figure 6.1c.

Figures 6.1a can be expressed as following:

$$w_a(\rho) = w_0 \times \frac{\rho_0/\rho - \phi_c}{1-\phi_c} \qquad (6.4)$$

where w_0 is the original vessel width, ρ_0 is the aspen oven-dried density, ϕ_c is the cell wall area fraction of aspen, ρ is the oven-dried density of oriented strand-based wood composites, $w(\rho)$ is the vessel width at a density of ρ.

Figure 6.1c can be expressed as following:

$$w_c(\rho) = w_0 \times \frac{\rho_0 / \rho - \phi_c - \phi_f}{1 - \phi_c - \phi_f} \tag{6.5}$$

where ϕ_f is the lumen area fraction of aspen.

With the average oven-dried density of aspen (403.87 kg/m^3, Avramidis and Mansfield 2005), parameters in Table 6.1, and Equation 6.3, Figures 6.1a and 6.1c are plotted below. $w_c(\rho) = 0$ when the density is 599.21 kg/m^3.

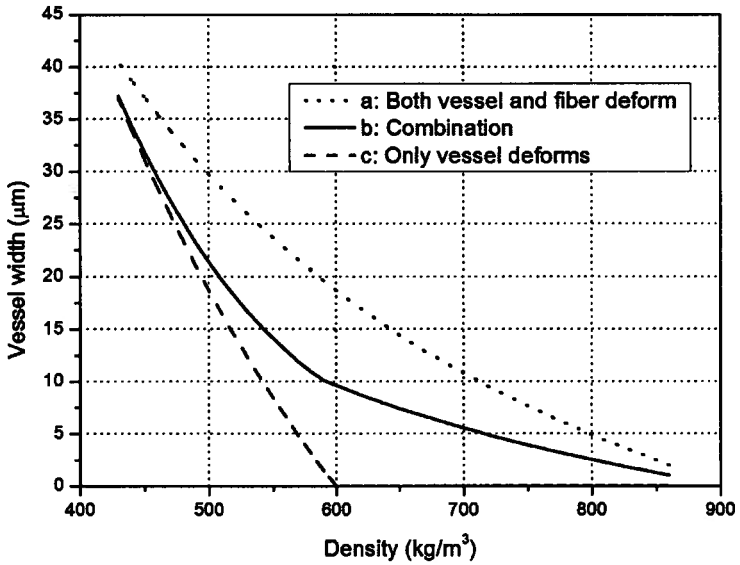

Figure 6.1: The development of vessel width as density increases: (a) vessels and fibers deform simultaneously throughout the compression; (b) combination of development pattern (a) and (c); (c) only vessels deform while fibers maintain their original sizes.

The microscopic investigation in Chapter 5 indicates that the real vessel deformation falls between the two extreme conditions, shown in Figure 6.1b: at the beginning type (c) dominates; while the density increases both types contributes; finally vessel lumens deform following type (a) after the type (c) decreases to 0.

Based on that, it is assumed that the contribution of type (a) and type (c) to the vessel deformation is equal after the density increases to 599.2 kg/m^3. Before this threshold, the contribution of type (c) linearly decreases from 100% to 50%, while the contribution of type (a) linearly increases from 0% to 50%. Because after 599.2 kg/m^3 $w_c(\rho) = 0$, the

change of vessel width actually follows Equation 6.4. Therefore, Figure 6.1b is expressed as:

$$w(\rho) = w_a(\rho) \times \alpha_a + w_c(\rho) \times \alpha_c \tag{6.6}$$

where α_a and α_c are the coefficient of type (a) and type (c) deformation, representing their contribution to the vessel width changes.

Assume that the compression starts when the mat density equals to the original aspen density 403.87 kg/m^3, at this point $\alpha_a = 0$ and $\alpha_c = 1$, combined with the boundary conditions at 599.2 kg/m^3, α_a and α_c can be calculated as:

$$\begin{gathered} \alpha_a = -0.00255 \times \rho + 2.0236, \alpha_c = 0.00255 \times \rho - 1.0236 \text{ when } \rho \le 599.21 \text{ kg/m}^3 \\ \alpha_a = \alpha_c = 0.5 \text{ when } \rho > 599.21 \text{ kg/m}^3 \end{gathered} \tag{6.7}$$

The vessel width is obtained in Equation 6.6. According to Equation 6.2, the volumetric rate in each micro-channel at density ρ is calculated as:

$$Q_i / t = \frac{w_0 (w(\rho))^3}{12\eta} \frac{\Delta p}{L} \left(1 - \frac{192 w(\rho)}{\pi^5 w_0} \sum_{n=1,3,\ldots}^{\infty} \frac{\tanh(n\pi w_0 / (2w(\rho)))}{n^5} \right) \tag{6.8}$$

The number of vessel elements in a unit area of aspen transverse cross section is calculated as:

$$N_a = (A_v / A_{v0}) / A = \phi_v / A_{v0} \tag{6.9}$$

$$A_{v0} = \pi D_0^{\,2} / 4 \tag{6.10}$$

where ϕ_v is the vessel lumen area fraction (values in Table 6.1), A_v is the area of vessel lumens in area A (mm^2), A_{v0} is the area of a vessel lumen (mm^2), D_0 is the initial vessel lumen diameter (μm). For oriented strand-based wood composites with density ρ (kg/m^3), the number of vessel elements per unit area is:

$$N = N_a \times (\rho / \rho_0) \tag{6.11}$$

where ρ_0 is the density of aspen (kg/m^3), and N has a unit of mm^{-2}.

Sum of the volumetric rate in all micro-channels is:

$$Q/t = (Q_i/t) \times A \times N \tag{6.12}$$

Permeability calculation based on Darcy's law can be written as:

$$K = k\eta = \frac{(Q/t) \times L}{A \times \Delta p}\eta \tag{6.13}$$

Note that Δp (Pa), A (mm^2), and L (mm) refer to the pressure drop across, cross-sectional area of and the length of the overall sample.

Substitute Equations 6.8 and 6.12, Equation 6.13 becomes:

$$K = \frac{w_0(w(\rho))^3}{12}\frac{\Delta p}{L}\left(1 - \frac{192w(\rho)}{\pi^5 w_0}\sum_{n=1,3,\ldots}^{\infty}\frac{\tanh(n\pi w_0/(2w(\rho)))}{n^5}\right) \times N \Big/ (\Delta p/L) \tag{6.14}$$

The reason not eliminating $\Delta p/L$ is that the first Δp and L will be modified when adding strand boundary and inter-strand effects.

6.2.2 Flow through strand boundaries

Since the strands have a limited length and are oriented to form a panel, the fluid cannot flow through one vessel element from one end of the board to the other; it will be interrupted at the end of each strand. Examination of a panel section, as shown in Figure 6.2, shows that the end of one strand contacts with the surface of the adjacent strands.

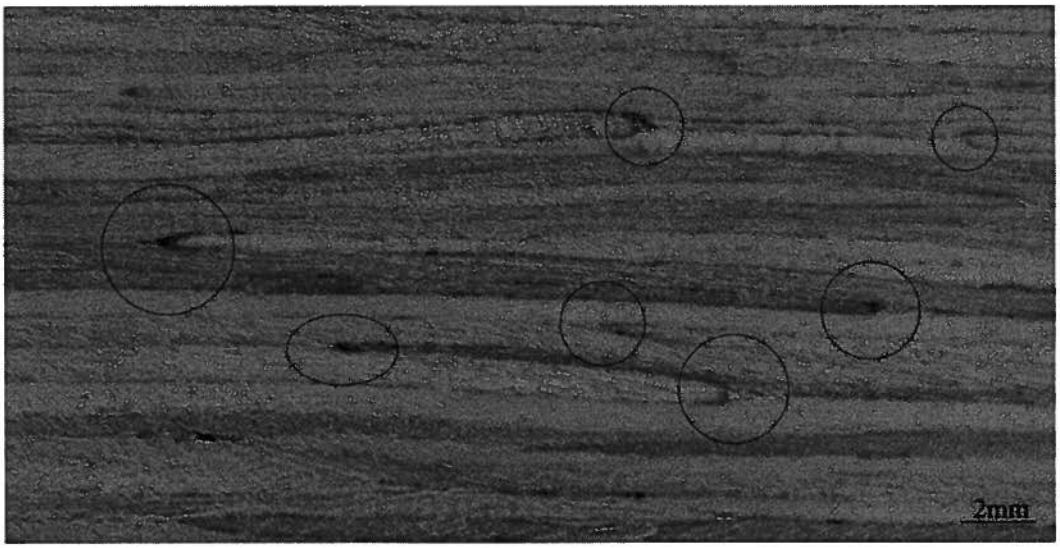

Figure 6.2: Examples of strand boundaries at the end of one strand: the plane is cut through thickness and parallel to strand orientation.

In Figure 6.3, a short section of oriented strand-based wood composite is selected and the longitudinal flow indicated by arrows. As the longitudinal permeability is much higher than the transverse permeability (Siau 1995), Strand A has a lower pressure gradient than B and C. The pressure drop of the four strands is also plot. Between O and X_2, Strand A has higher pressure than B and C which creates perpendicular flow. The same phenomenon happens between B and D, C and E. A two dimensional flow representing the real flow pattern is shown in Figure 6.3c.

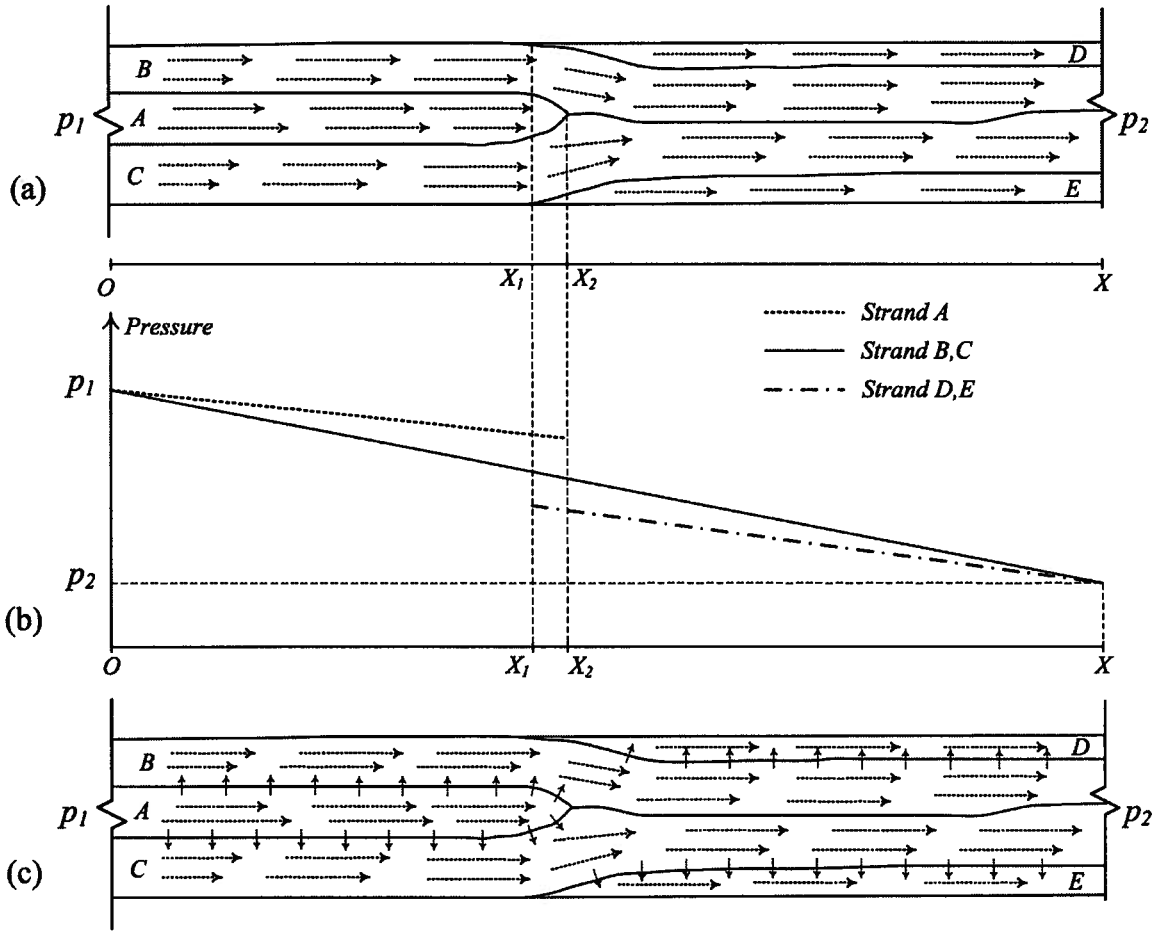

Figure 6.3: Flow and pressure drop caused by strand joints.

For a small amount of fluid starting at Strand A, a possible path is that it flows longitudinally through A, then transversely to B or C, and continuously flows longitudinally in B or C until the end. During this process flow occurs in both directions

parallel and perpendicular to the strand orientation. It includes the longitudinal flow in the vessel and the transverse flow at the end of strands. But only the flow parallel to the strand orientation contributes to the overall permeability when investigating a single cross section.

Based on this, the flow path of oriented strand-based wood composites can be simplified by arranging longitudinal flow and transverse flow in series. In oriented strand wood composites, the flow in vessels is separated by short intervals of transverse transportation with significantly lower permeability as shown schematically in Figure 6.4.

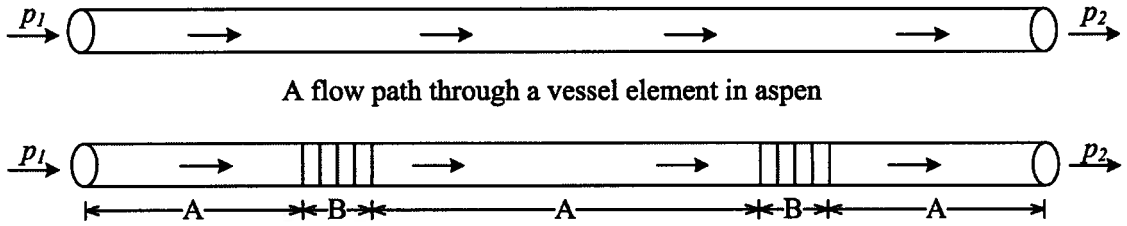

A flow path through a vessel element in aspen

A flow path in an oriented strand wood composite

A: Flow in longitudinal direction; B: Flow in transverse direction. B is the lower permeability part

Figure 6.4: Individual flow path comparison in aspen and oriented strand wood composites.

In Figure 6.4, part A and part B have the same fluid volumetric flow rate $Q/A=C$. According to Darcy's law in Equation 6.15, the pressure gradient is inversely proportional to the cross sectional area and permeability. The existence of transverse flow creates the low permeability parts with a higher pressure gradient which leads to a decreased pressure gradient in longitudinal flows. Figure 6.5 shows the pressure changes along the two flow paths in Figure 6.4.

$$k = \frac{Q\,\Delta L}{t\,A\,\Delta p} \quad \Rightarrow \quad \frac{\Delta p}{\Delta L} = \frac{Q}{t\,A\,k} = \frac{C}{A\,k} \tag{6.15}$$

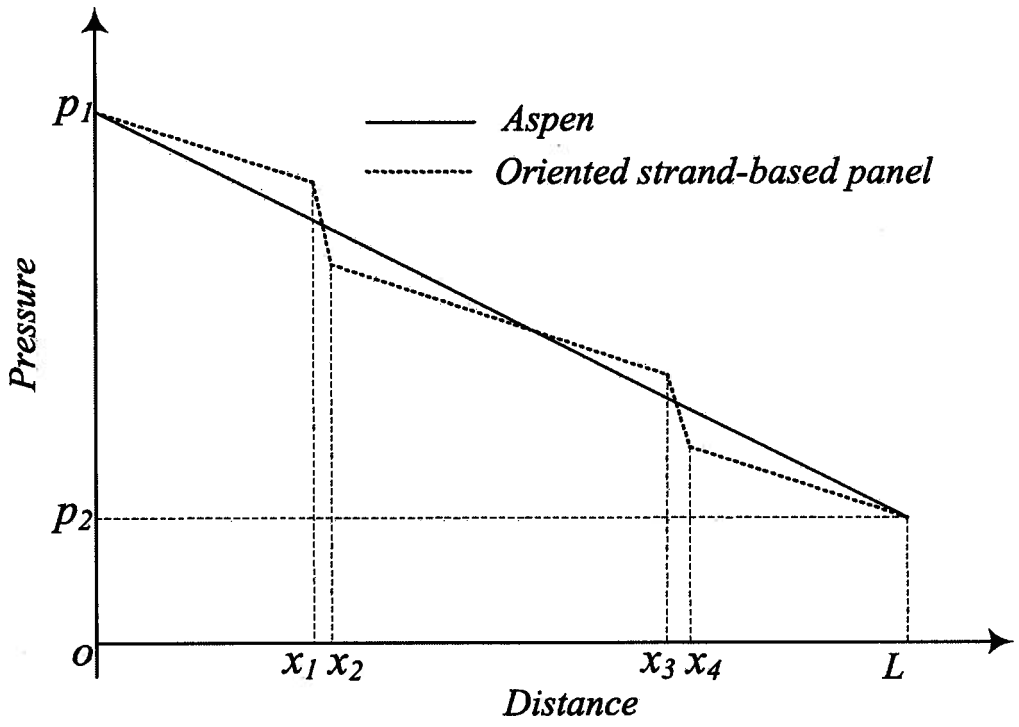

Figure 6.5: Pressure drop along the flow path in aspen and an oriented strand-based panel.

Comparing the two kinds of flow paths, the effect of strand boundaries is to create a lower fluid volumetric flow rate which leads to a decreased permeability for the whole sample. And the shorter strands are, the more transverse penetrations the flow has to pass through, the lower permeability it will be.

For the flow path of oriented strand wood composites in Figure 6.4, it has the following relationship from Equation 6.15:

$$\frac{\Delta p_A}{\Delta L_A} \times A_A \times k_A = \frac{\Delta p_B}{\Delta L_B} \times A_B \times k_B \qquad (6.16)$$

$$\Delta p_A + \Delta p_B = \Delta p = p_1 - p_2 \qquad (6.17)$$

To obtain the average pressure gradient in the longitudinal direction in order to calculate the volumetric flow rate, the following assumptions are made.

Assuming all the strands are uniformly compressed, it can be considered:

$$A_A = A_B \qquad (6.18)$$

According to the value of the longitudinal and transverse permeability of aspen provided by Siau (1995), the ratio of k_A/k_B is estimated to be 100.

The sum of the length of all Part A and Part B is the overall sample length (203.2mm). When the fluid flows from one strand perpendicularly to the adjacent strands, the longest path equals to the strand thickness 1mm (from strand center to strand center), and the shortest is 0 (from strand edge to strand edge). Therefore, the average length of each low permeability section is considered as half of the strand thickness t_{tr}=0.5mm.

The average length of strands is 152.4mm, which is 75% of the whole sample length. There are three common types of strand alignments yielding different times of transverse flow when fluid passes from one end of the sample to the other, as shown in Figure 6.6.

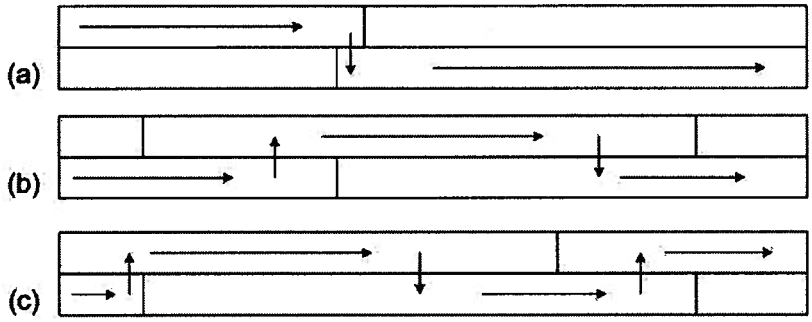

Figure 6.6: Different times of transverse flows created by various strand alignments: (a) one transverse flow, (b) two transverse flows, and (c) three transverse flows.

It is difficult to determine the percentages of each alignment type in a sample. In addition, the existence of short strands makes it more complex. To simplify the problem, it is assumed that on average there are n_{tr}=2 low permeability sections per micro-flow path.

$$\Delta L_A = 203.2, \Delta L_B = n_{tr} \times t_{tr} = 1.0 \qquad (6.19)$$

With these values Equations 6.16 and 6.17 yield the following result:

$$\Delta p_A = 2.032 \times \Delta p_B \Rightarrow \Delta p_A = 0.670 \times (p_1 - p_2) \qquad (6.20)$$

Δp_A is also defined as effective pressure drop with an coefficient c:

$$\Delta p_e = c \times (p_1 - p_2) \qquad (6.21)$$

In this case, coefficient c equals to 0.670.

Therefore, Equation 6.14 becomes:

$$K = \frac{w_0(w(\rho))^3}{12}\frac{\Delta p_e}{\Delta p}\left(1-\frac{192w(\rho)}{\pi^5 w_0}\sum_{n=1,3,\ldots}^{\infty}\frac{\tanh(n\pi w_0/(2w(\rho)))}{n^5}\right)\times N \qquad (6.22)$$

6.3 Effects of inter-strand voids

From macroscopic and microscopic observations in Chapter 5, inter-strand voids have a significant existence in 450 kg/m^3 samples with a large cross sectional size and long length. But none of them is found to cross through even half the sample length. The other four density samples have a much smaller void size and quantity.

The inter-strand voids are trapped among a pile of strands. Because of their large size and length, the voids provide an express route for the fluid flow. And the pressure change inside such a void is negligible compared with that occurring inside a strand. Therefore, the effect of inter-strand flow is decreasing the path length of intra-strand flow by creating a section of very low pressure gradient, as shown in Figure 6.7. Because of its high permeability the pressure gradient created by inter-strand voids is negligible in the calculation.

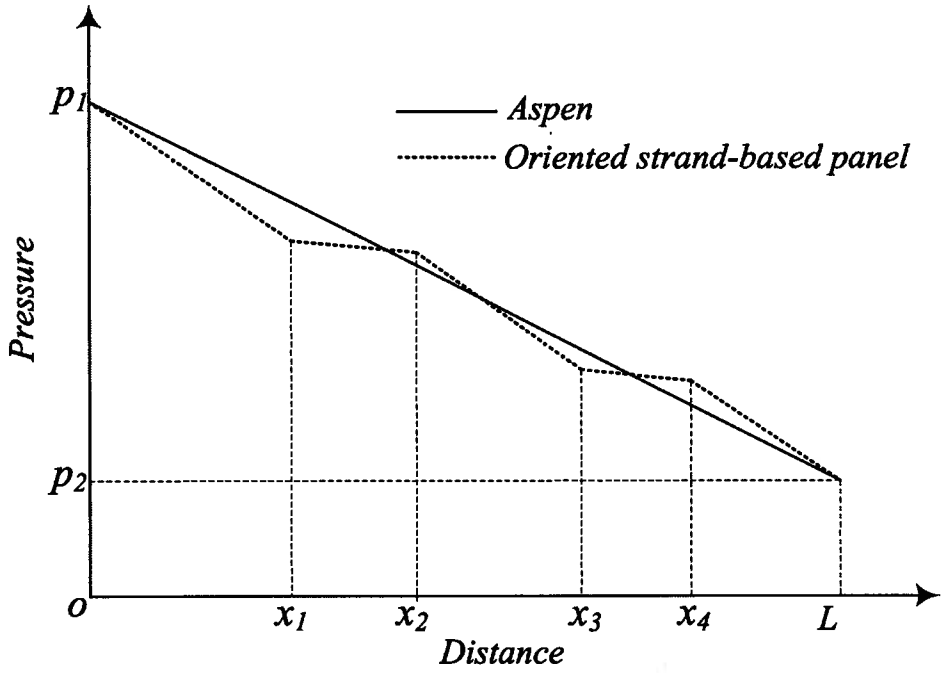

Figure 6.7: Pressure drop change by adding the effect of inter-strand voids.

According to this phenomenon the flow path in oriented strand-based wood composites can be represented schematically as shown in Figure 6.8.

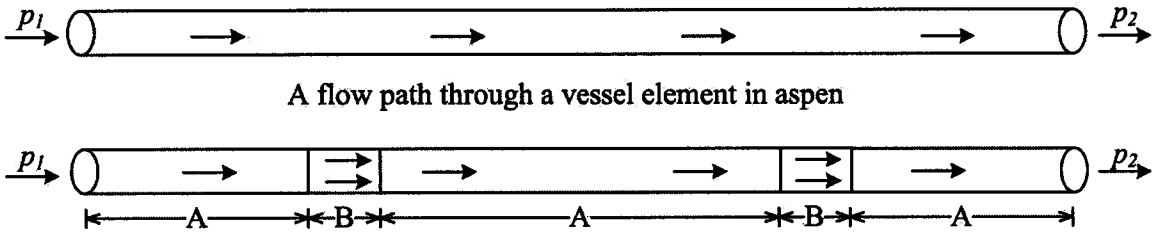

A: Flow in an vessel of a strand; B: Flow in inter-strand voids. B is the higher permeability part

Figure 6.8: Flow path change by adding the effect of inter-strand voids.

The sample length is 203.2 mm and strand length is 152.4 mm. When the oriented strand wood composite is loosely compressed to a density as the same as aspen (403.87 kg/m^3), one continuous inter-strand void has a length of 152.4 mm, which is bridged by the adjacent strands. The average inter-strand void length is assumed as 152.4 mm which is 75% of the overall sample length.

According to the microscopic investigation, in samples of above 625 kg/m^3, inter-strand voids are small and the length is less than 0.5% of the sample (voids are shorter than 1mm, compared with a sample length of 203.2 mm). Therefore, the contribution of inter-strand voids to the fluid flow of the overall sample is so small that this part can be neglected in the calculation.

Assume that the length fraction φ_{inter} of inter-strand voids to the overall sample decreases from 75% at 403.87 kg/m^3 to 0.5% at 625 kg/m^3, it can be expressed as:

$$\phi_{\text{inter}} = f(\rho) \tag{6.23}$$

From Chapter 5, the length decreasing of inter-strand voids slows down as the density increases, therefore

$$\phi''_{\text{inter}} = f''(\rho) > 0 \tag{6.24}$$

At 625 kg/m^3, the length change of inter-strand voids is very small, which can be expressed as:

$$\phi'_{\text{inter}} = f'(\rho)\big|_{\rho=625} = 0 \tag{6.25}$$

The simplest equation that fulfills the boundary conditions above will be a second order polynomial:

$$\phi_{\text{inter}} = 1.524\times10^{-5}\times\rho^2 - 1.304\times10^{-2}\times\rho + 5.356 \tag{6.26}$$

The effective length for the flow path is:

$$L_e = L\times(1-\phi_{\text{inter}}) \tag{6.27}$$

The pressure drop remains:

$$\Delta p = p_1 - p_2 \tag{6.28}$$

To calculate the volumetric rate in each micro-channel, substituting Equations 6.26 and 6.27 into Equation 6.8 produces:

$$Q_i/t = \frac{w_0(w(\rho))^3}{12\eta}\frac{\Delta p}{L_e}\left(1-\frac{192w(\rho)}{\pi^5 w_0}\sum_{n=1,3,\ldots}^{\infty}\frac{\tanh\left(n\pi w_0/(2w(\rho))\right)}{n^5}\right) \tag{6.29}$$

The number of vessel elements per unit area is also calculated by Equation 6.11.

Therefore, Equation 6.14 becomes:

$$K = \frac{w_0(w(\rho))^3}{12}\frac{L}{L_e}\left(1-\frac{192w(\rho)}{\pi^5 w_0}\sum_{n=1,3,\ldots}^{\infty}\frac{\tanh(n\pi w_0/(2w(\rho)))}{n^5}\right)\times N \qquad (6.30).$$

6.4 Final model and validation

From the analysis in sections 6.2 and 6.3, below 625 kg/m^3 inter-strand voids serve as an express route for flow transportation by decreasing the path length as a result of its much higher permeability than vessels. While if higher than 625 kg/m^3, the inter-strand voids are close and the flow is forced to pass transversely into the next strand in order to continue forward. The result is that the pressure gradient in vessel elements is decreased because of the low permeability in transverse direction.

Therefore, below 625 kg/m^3 the effective length L_e is applied while the effective pressure drop Δp_e equals to the overall pressure drop Δp, and Equation 6.30 was used to predict permeability; for specimens with density higher than 625 kg/m^3, Δp_e needs to be accounted for, and Equation 6.22 was used. For convenience, the values used for each terms Equation 6.30 are listed below I

The experimental data and computed results are shown in Figure 6.9. The effect of intra-strand is also plotted to show the different contribution of inter- and intra-strand voids.

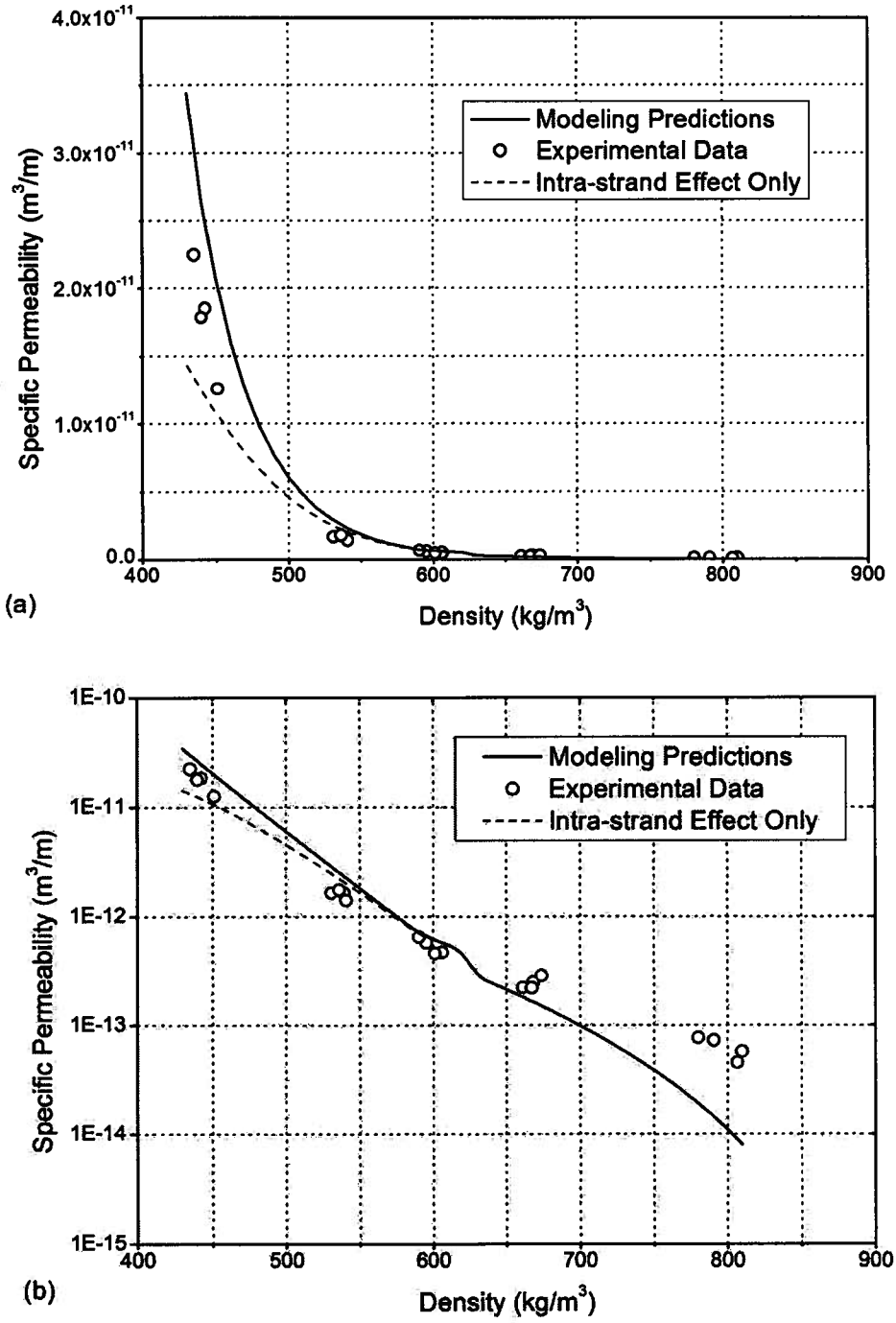

Figure 6.9: Experimental data and modeling estimated result (parallel to strand orientation): (a) plot with a linear y axis, (b) plot with a log-transformed y axis.

From 450 to 700 kg/m^3, the model has a good agreement with the experimental data; while for 800 kg/m^3 the model estimates are lower than the measurement but still in the same order of magnitude.

6.5 Discussion

As stated previously the variation of strand size, property, and lay-up results in non-uniformly distributed void sizes including both inter-strand and intra-strand. The model produces an overall average estimate of this complex phenomenon. From Equations 6.22 and 6.30, for higher density panels the existence of larger voids has a more significant effect on the overall permeability because permeability is proportional to the cubic of void height. This trend is also shown by the high density range in Figure 6.9. To add the effect of void size variation in the model, a measurement of void size distribution has to be performed, which requires enough high quality microscopic images covering an area fully representing the various compression stages of the sample.

The inter-strand effect decreases from a significant level to almost negligible as the density increases, which occurs in a density range. Because of lacking information, it is difficult to determine the beginning and end of this range, as well as how it changes across the range. The model selects a point approaching to the end of this transition interval, 625 kg/m^3, to represent the change of inter-strand effect. Therefore, in the model prediction, the curve close to 625 kg/m^3 is not as smooth as the other parts.

In the model all strands are assumed to be of the same size. In the production of commercial strand-based wood composites the strands have various kinds of shapes and size. The interaction between inter-strand and intra-strand flow will be more complex than described by the model. Industrial automatic lay-up processes will likely have more variability in void size than the laboratory hand forming method used here.

The effects of resin content and moisture content are not included in the modeling as there is no information on how the presence of resin affects permeability. Presumably, as the resin content increases it becomes progressively more difficult for the gases to flow through the strands. Whether the resin has a preference of strand scale or fiber scale features that will affect gas flow in these directions is not known. The validation of this

model also needs to be performed on other kinds of oriented strand-based wood composites to ensure the model is generally applicable.

7 Summary, Conclusions, and Recommendations

7.1 Summary and conclusions

This research investigated the in-plane permeability of oriented strand-based wood composites, which is a key factor controlling the heat-mass transfer process and affecting the energy consumption during the manufacturing.

To measure the in-plane permeability of a large size sample in three directions, a specimen holder that could seal samples well inside was designed and tested. It was able to provide reliable results in combination with the permeability apparatus. Five densities of oriented strand-based wood panels were manufactured with four replicates for each level, and then cut into the required sizes for permeability and VDP testing. The VDP test showed that the panel had a constant density profile to ensure the permeability value was valid for the targeted density. Permeability values decreased rapidly as the density increased. Permeability was greatest in the parallel-to-strand direction, and lowest in the perpendicular-to-strand direction. Permeability values in 45° direction were between the measurements of parallel- and perpendicular-to-strand directions.

Microscopic techniques were used to determine the changes in inter-strand and intra-strand voids during compression. A method to prepare slides for wood composite was developed and yielded clear images in a transmitted light microscope. Inter-strand voids decreased significantly with density and after 625 kg/m^3, its effect could be neglected. A large variation occurred when comparing the compression stages of different specimens. Even for one strand, the compression of vessel elements was not uniform. The images obtained also revealed the development of intra-strand voids during compression, including the cell wall failure pattern, vessel-fiber system deformation, and the strand behavior with different cutting orientations.

Finally a mechanistic model was developed to predict the permeability of oriented strand-based wood composites according to its microscopic and macroscopic geometry investigations. As strands with various compression stages yield panels with a specific density, an average compression stage was chosen to represent the complex states in a

board. The vessel elements inside the strands were considered as the main path for flow transportation, which could be assumed as a pipe with a constant cross sectional size. The original vessel size and its quantity were obtained from previous work. And a relationship was established to calculate the vessel size at a given density level. The effect of inter-strand voids was also incorporated into the model. Below a threshold density, the main effect of compression was to decrease the length of intra-strand transportation. Above the threshold, permeability decreases as the effect becomes decreasing the pressure gradient in vessels by forcing longitudinal transportation to transverse transportation. When validating the model with the experimental data, it yielded a good agreement except at the highest density range.

7.2 Recommendations

Future research includes the validation of the current model on other type of oriented strand-based wood composites; add more parameters, e.g., moisture content, resin content into the model; and link the results with the in-situ measurements. The relationship between flow transportation and micro-void distribution could be improved with some new techniques. Micro-CT (Computed Tomography) is able to provide a non-destructive three dimensional void structures of porous media with void size as small as 5μm. Applying the electrical permeability measuring apparatus will also make the measurement of large quantity of samples in a short time possible, which means more variables can be added and investigated to have a clearer and more comprehensive understanding of permeability in wood composites.

References

APA. 2007. Regional Production and Market Outlook, 2007-2012. APA-The Engineered Wood Association.

Avramidis, S., and Mansfield, S.D. 2005. On some physical properties of six aspen clones. Holzforschung 59(1): 54-58.

Blair, S., Berge, P., and Berryman, J. 1996. Using two-point correlation functions to characterize microgeometry and estimate permeabilities of sandstones and porous glass. Journal of Geophysical Research 101(B9): 20359-20376.

Bolton, A.J., and Humphrey, P.E. 1994. The permeability of wood-based composite materials. I: A review of the literature and some unpublished work. de Gruyter. pp. 95-100.

Bolton, A.J., Humphrey, P.E., and Kavvouras, P.K. 1988. The hot pressing of dry-formed wood-based composites. Part 1: a review of the literature, identifying the primary physical processes and the nature of their interaction. Holzforschung 42(6): 403-406.

Bolton, A.J., Humphrey, P.E., and Kavvouras, P.K. 1989a. The hot pressing of dry-formed wood-based composites. IV: Predicted variation of mattress moisture content with time. Holzforschung 43(5): 345-349.

Bolton, A.J., Humphrey, P.E., and Kavvouras, P.K. 1989b. The hot pressing of dry-formed wood-based composites. Part. 3: Predicted vapour pressure and temperature variation with time, compared with experimental data for laboratory boards. Holzforschung 43(4): 265-274.

Bowen, M.E. 1970. Heat Transfer in particleboard during hot pressing. PhD Thesis. Colorado State University, Corvallis, United States. 114 pp.

Carvalho, L.M.H., and Costa, C.A.V. 1998. Modeling and simulation of the hot-pressing process in the production of medium density fiberboard (MDF). Chemical Engineering Communications 170(1): 1-21.

Carvalho, L.M.H., Costa, M.R.N., and Costa, C.A.V. 2003. A global model for the hot-pressing of MDF. Wood Science and Technology 37(3): 241-258.

Dai, C., and Yu, C. 2004. Heat and mass transfer in wood composite panels during hot-pressing. Part I. A physical mathematical model. Wood and Fiber Science 36(34): 585-597.

Dai, C., Yu, C., and Zhou, X. 2005. Heat and mass transfer in wood composite panels during hot pressing. Part II. Modeling void formation and mat permeability. Wood Fiber Sci 37(2): 242-257.

Denisov, O.B., and Sosnin, M.S. 1967. Characterization of changing temperature and steam pressure inside a particleboard mat during pressing (In Russian). Derev. Prom 16(8): 11.

Denny, M.W. 1993. Air and Water: The Biology and Physics of Life's Media. Princeton Univ Pr.

Fakhri, H., Semple, K., and Smith, G. 2006a. Permeability of OSB. Part I. The Effects of Core Fines Content and Mat Density on Transverse Permeability. Wood and Fiber Science 38(3): 450-462.

Fakhri, H., Semple, K., and Smith, G. 2006b. Transverse Permeability of OSB. Part II. Modeling the Effects of Density and Core Fines Content. Wood and Fiber Science 38(3): 463-473.

Flannery, B.P., Deckman, H.W., Roberge, W.G., and D'Amico, K.L. 1987. Three-Dimensional X-ray Microtomography. Science 237(4821): 1439-1444.

Garcia, P.J. 2002. Three dimensional heat and mass transfer during oriented strandboard hot-pressing. PhD thesis. University of British Columbia, Canada.

Garcia, P.J, Avramidis, S., and Lam, F. 2001. Internal temperature and pressure responses to flake alignment during hot-pressing. Holz als Roh- und Werkstoff59 (4): 272-275.

Garcia, P.J, Avramidis, S., and Lam, F. 2003. Horizontal gas pressure and temperature distribution responses to OSB flake alignment during hot-pressing. Holz als Roh- und Werkstoff 61(6): 425-431.

Garcia, P.J, Avramidis, S., and Lam, F. 2004. Regression modeling of two-dimensional internal temperature and gas pressure distributions during panel hot-pressing. Holz als Roh- und Werkstoff 62(4): 316-320.

Garcia, R., and Cloutier, A. 2005. Characterization of Heat and Mass Transfer in the Mat during the Hot Pressing of MDF Panels. Wood and Fiber Science 37(1): 23-41.

Geimer, R.L., and Forest Products, L. 1985. Influence of Processing-induced Damage on Strength of Flakes and Flakeboards. US Dept. of Agriculture, Forest Service, Forest Products Laboratory.

Haas, G. 1998. Investigations of the hot-pressing of wood composite mats under special consideration of the compression behavior, the permeability, the temperature conductivity and the sorption speed. (In German). University of Hamburg, Germany.

Handbook, W. 1999. Wood Handbook - Wood as an engineering material. Department of Agriculture, Forest Service, Forest Products Laboratory, U.S.

Hata, T. 1993. Heat Flow in Particle Mat and Properties of Particleboard under Steam-Injection Pressing. Wood Research 80: 1-47.

Hood, J.P. 2004. Changes in oriented strandboard permeability during hot-pressing. MSc Thesis, Virginia Polytechnic Institute, Blacksgurg, VA. 85pp.

Hood, J.P., Kamke, F.A., and Fuller, J. 2005. Permeability of oriented strandboard mats. Forest Products Journal 55(12): 194-199.

Humphrey, P., and Bolton, A.J. 1989. The hot pressing of dry formed wood-based composites. Part 2. Simulation model for heat and moisture transfer, and typical results. Holzforschung 43(3): 199-206.

Jana, D. 2006. sample preparation techniques in petrographic examination of construction materials: a state of the art review. In Twenty-eigth conference on cement microscopy, Denver, Colorado, USA.

Jung, J.Y., and Kwak, H.Y. 2008. Fluid flow and heat transfer in microchannels with rectangular cross section. Heat Mass Transfer 44: 1041-1049.

Kamke, F. 2007. Short course: OSB fundamentals Dept. Wood Science and Engineering, Oregon State University.

Kamke, F.A., and Zylkowski, S.C. 1989. Effects of wood-based panel characteristics on thermal conductivity. Forest products journal 39(5): 19-24.

Kavvouras, P.K. 1977. Fundamental process variables in particleboard manufacture. University of Wales, Bangor, UK.

Kostiainen, K., Kaakinen, S., Warsta, E., Kubiske, M.E., Nelson, N.D., Sober, J., Karnosky, D.F., Saranpaa, P., and Vapaavuori, E. 2008. Wood properties of trembling aspen and paper birch after 5 years of exposure to elevated concentrations of CO2 and CO3. Tree Physiology. pp. 805-813.

Kultikova, E.V. 1999. Structure and Properties Relationships of Densified Wood. Virginia Polytechnic Institute and State University, Blacksburg, Virginia.

Lu, S., Landis, E., and Keane, D. 2006. X-ray microtomographic studies of pore structure and permeability in Portland cement concrete. Materials and Structures 39(6): 611-620.

Müller, U., Gindl, W., and Teischinger, A. 2003. Effects of cell anatomy on the plastic and elastic behavior of different wood species loaded perpendicular to grain. IAWA Journal 24(2): 117-128.

Muskat, M. 1946. The Flow of Homogenous Fluids Through Porous Media. JW Edwards. Ann Arbor.

Oudjehane, A., and Lam, F. 1998. On the density profile within random and oriented wood-based composite panels: Horizontal distribution. Composites Part B, 29B: 687-694.

Oudjehane, A., Lam, F., and Avramidis, S. 1998a. Forming and pressing processes of random and oriented wood composite mats. Composites Part B, 29B: 211-215.

Oudjehane, A., Lam, F., Avramidis, S. 1998b. A continuum model of the interaction between manufacturing variables and consolidation of wood composite mats. Wood Science and Technology 32: 381-391.

Panshin, A.J., and de Zeeuw, C. 1980. Textbook of Wood Technology. 4th edition. McGraw-Hill Book Company, New York.

Panshin, A.J., and Zeeuw, D.E. 1970. Textbook of Wood Technology Volume 1. Structure, identification, uses, and properties of the commercial woods of the United States and of Canada. McGraw-Hill Book Company, New York.

Random Lengths. 2008. Random Lengths 2007 yearbook: forest product market and statistics. Random Lengths publications, Inc. Eugene, OR.

RISI. 2008 December: North American Wood Panels Forecast – Excerpt. Boston, Massachusetts, USA.

Rohsenow, W.M., Hartnett, J.P., and Cho, Y.I. 1998. Handbook of Heat Transfer. McGraw-Hill Professional.

Schaap, M.G., and Lebron, I. 2001. Using microscope observations of thin sections to estimate soil permeability with the Kozeny-Carman equation. Journal of Hydrology 251(3-4): 186-201.

Scheidegger, A.E. 1974. The physics of flow through porous media. University of Toronto Press, Toronto.

Shida, S., and Okuma, M. 1981. The effect of the apparent specific gravity on thermal conductivity of particleboard. Mokuzai Gakkaishi 27: 775-781.

Siau, J.F. 1995. Wood: influence of moisture on physical properties. Dept. of Wood Science and Forest Products, Virginia Polytechnic Institute and State University.

Sokunbi, O.K. 1978. Aspects of particleboard permeability. Master's thesis, University of Wales, UK.

Spelter, H., McKeever, D., and Alderman, M. 2006. Status and Trends: Profile of Structural Panels in the United States and Canada. Res. Pap. FPL-RP-636. US For. Serv. Forest Products Lab., Madison, WI.

Strickler, M.D. 1959. The effect of press cycles and moisture content on properties of Douglas fir flakeboard. Forest Prod. J 9(7): 203-215.

Sugimori, M., and Lam, F. 1999. Macro-void distribution analysis in strand-based wood composites using an X-ray computer tomography technique. Journal of Wood Science 45(3): 254-257.

Sutton, A., and Tardif, J. 2005. Distribution and anatomical characteristics of white rings in Populus tremuloides. IAWA Journal 26(2): 221-238.

Suzuki, M. 1981. Physical characteristics of multilayer particleboard. Mokuzai Gakkaishi 27(5).

Tabarsa, T., and Chui, Y.H. 2000. Stress-strain response of wood under radial compression. Part I. Test method and influences of cellular properties. Wood and Fiber Science 32(2): 144-152.

Tabarsa, T., and Chui, Y.H. 2001. Characterizing microscopic behavior of wood under transverse compression. Part II. Effect of species and loading direction. Wood and Fiber Science 33(2): 223-232.

Thoemen, H. 2000. Modeling the physical processes in natural fiber composites during batch and continuous pressing. PhD thesis, Oregon State University, Corvallis, OR.

Thoemen, H., Haselein, C.R., and Humphrey, P.E. 2006. Modeling the physical processes relevant during hot pressing of wood-based composites. Part II. Rheology. Holz als Roh- und Werkstoff 64(2): 125-133.

Thoemen, H., and Humphrey, P. 2003. Modeling the Continuous Pressing Process for Wood-Based Composites. Wood and Fiber Science 35(3): 456-468.

Thoemen, H., and Humphrey, P.E. 2006. Modeling the physical processes relevant during hot pressing of wood-based composites. Part I. Heat and mass transfer. Holz als Roh- und Werkstoff 64(1): 1-10.

Thoemen, H., and Klueppel, A. 2008. An investigation on the permeability of different wood furnish materials. Holzforschung 62(2): 215-222.

UNECE. 2009. Timber Committee Market Statement on Forest Products Markets in 2008 and 2009. United Nations Economic Commission for Europe. Geneva, Switzerland.

UNECE/FAO. 2007. Forest Products Annual Market Review 2006-2007. United Nations Economic Commission for Europe / Food and Agriculture Organization of the United Nations. Geneva, Switzerland.

UNECE/FAO. 2008. Forest Products Annual Market Review 2007-2008. United Nations Economic Commission for Europe / Food and Agriculture Organization of the United Nations. Geneva, Switzerland.

Wang, B.J., Zhou, X., Dai, C., and Ellis, S. 2006. Air permeability of aspen veneer and glueline: Experimentation and implications. Holzforschung 60(3): 304.

WBPI. 2008. OSB world survey. In Wood Based Panels International. pp. 14-23.

Zhang, B., Wu, Q., Wang, L., and Han, G. 2005. Characterization of Internal Void Structure of Strand-Based Wood Composites Using X-Ray Tomography and Digital Tools. In Proc. The McMat2005 – The 2005 joint ASME/ASCE/SES Conference on Mechanics and Materials. June 1-3, 2005. Baton Rouge, LA. Paper 257.

Zombori, B., Kamke, F., and Watson, L. 2003. Simulation of the Internal Conditions During The Hot-Pressing Process. Wood and Fiber Science 35(1): 2-23.

Appendix A: Preliminary Measurement on Commercial LSL

The purpose of preliminary measurements on commercial LSL samples is to obtain typical permeability values for commercially manufactured thick strand-based wood composites, and enable comparison with permeability values obtained for controlled density profile thick strand boards produced in the laboratory.

The commercial LSL was available in two density levels (580 and 690 kg/m^3) and four permeability specimens were cut and measured for each density. For each panel, permeability specimens representing three different directions were measured: parallel- and perpendicular-to-strand orientation, and 45° to strand orientation.

The original sizes of panels available in the laboratory were 558.8 mm by 454.0 mm by 31.8 mm and 101.6 mm by 352.4 mm by 44.5 mm. The thick panels were sanded down to 31.8 mm. Two panels were randomly selected from one density and each was cut into 2 permeability specimens measuring 203.2 mm by 203.2 mm by 31.8 mm. The measurement procedures and analysis methods were the same as those described in Chapter 3.

The permeability results are shown in Table A-1 and plot in Figure A-1. Before ANOVA test, the distribution of permeability values was checked by Ryan-Joiner normality test. The initial permeability values were not normally distributed (p<0.010). Therefore they were transformed using $\log_{10}$ and were then found to be normally distributed (p>0.100). Both density and direction of air flow significantly affected permeability (p<0.001), however, the interaction between these factors was not significant (p=0.647). Tukey's HSD test indicated that permeability values for each direction were significantly different (all p<0.001).

Table A.1: Permeability measurement results for commercial LSL samples.

Sample	Oven-dried density (kg/m^3)	Density level	K (0°)* m^3/m	K(90°)* m^3/m	K(45°)* m^3/m
1-1-1	557.5	1	9.10E-12	1.05E-12	2.92E-12
1-1-2	583.4	1	4.08E-12	5.92E-13	1.52E-12
1-2-1	587.2	1	4.00E-12	8.52E-13	1.76E-12
1-2-2	543.0	1	8.80E-12	2.83E-12	5.81E-12
2-1-1	712.9	2	6.31E-13	4.34E-14	1.57E-13
2-1-2	693.1	2	6.15E-13	7.49E-14	1.29E-13
2-2-1	706.0	2	4.10E-13	8.63E-14	2.07E-13
2-2-2	734.2	2	2.35E-13	7.29E-14	9.91E-14

* 0°, 90°, 45° mean the direction between air flow and strand alignment.

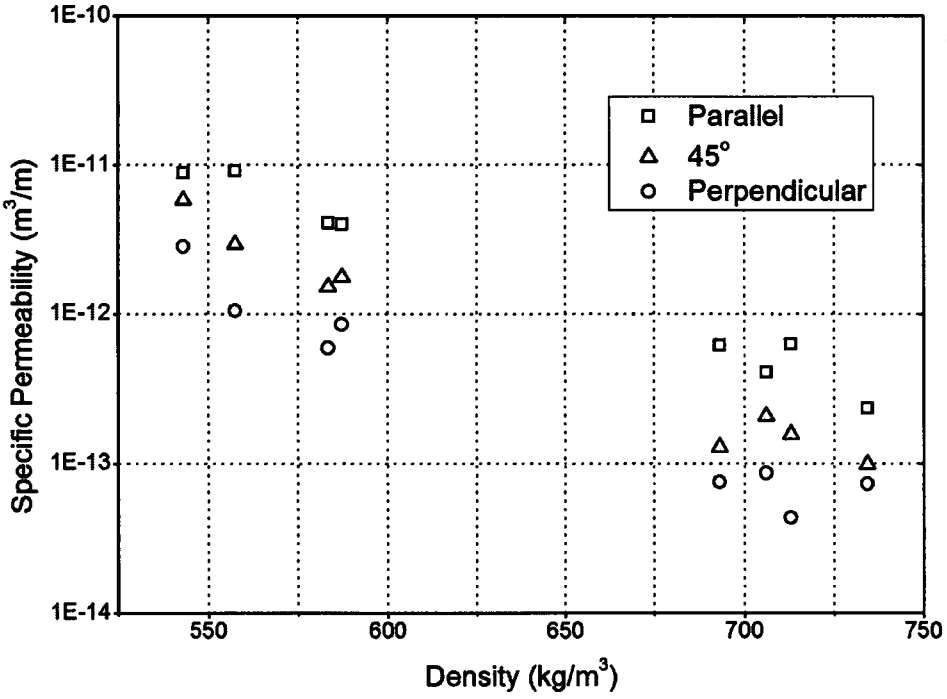

Figure A.1: Permeability measurement results for commercial LSL samples.

It is not necessary to perform a regression on the results since only two density levels were measured. The measurements on commercial LSL panels provided a preliminary insight into permeability readings for thick, strand-based wood composites. It also refined the process of specimen preparation and measuring to establish the methodology for permeability measurement of laboratory produced panels.

Appendix B: Summary of Statistical Analysis

Table B.1: One-way ANOVA test at a significance level of 0.05: the effect of density on the permeability results in the direction parallel to strand orientation.

Source	DF	SS	MS	F	p	Significance
Density level	4	13.67285	3.41821	545.97	0.000	significant
Error	15	0.09391	0.00626			
Total	19	13.76676				

Table B.2: One-way ANOVA test at a significance level of 0.05: the effect of density on the permeability results in the direction 45° to strand orientation.

Source	DF	SS	MS	F	p	Significance
Density level	4	15.1371	3.7843	98.58	0.000	significant
Error	15	0.5758	0.0384			
Total	19	15.7129				

Table B.3: One-way ANOVA test at a significance level of 0.05: the effect of density on the permeability results in the direction perpendicular to strand orientation.

Source	DF	SS	MS	F	p	Significance
Density level	4	17.5308	4.3827	369.10	0.000	significant
Error	15	0.1781	0.0119			
Total	19	17.7089				

Table B.4: Mean, Standard deviation, and variance for permeability results (log_{10} transformed).

Direction		Target Density (kg/m^3)				
		450	550	625	700	800
Parallel	Mean	-10.757	-11.793	-12.274	-12.614	-13.209
	Standard Deviation	0.105	0.041	0.073	0.052	0.103
	Variance	0.011	0.002	0.005	0.003	0.011
45°	Mean	-11.417	-12.551	-13.134	-13.210	-14.048
	Standard Deviation	0.111	0.149	0.213	0.231	0.243
	Variance	0.012	0.022	0.045	0.053	0.059
Perpendicular	Mean	-11.756	-13.059	-13.631	-14.010	-14.468
	Standard Deviation	0.059	0.105	0.126	0.116	0.124
	Variance	0.003	0.011	0.016	0.014	0.015